SAND2020-3890R

CASL-U-2020-1946-000

Consortium for Advanced Simulation of LWRs

Separate Effects Validation for Subcooled Boiling in CTF

N. W. Porter[1] and L. N. Gilkey[1]

[1]Sandia National Laboratories (SNL)

31 March 2020

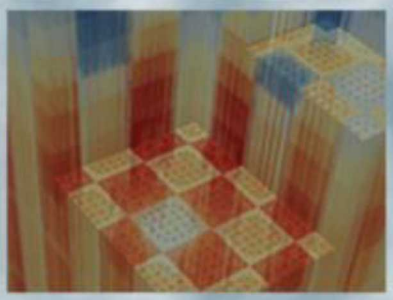

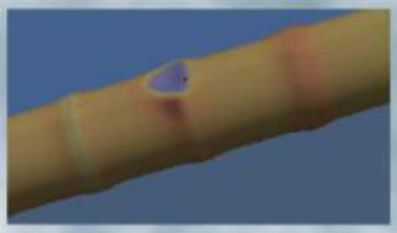

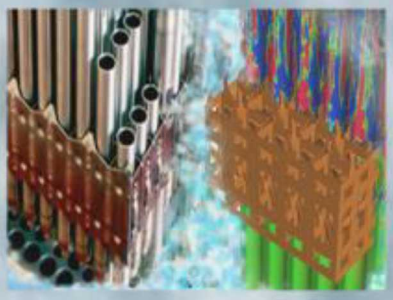

Sandia National Laboratories is a multimission laboratory managed and operated by National Technology & Engineering Solutions of Sandia, LLC, a wholly owned subsidiary of Honeywell International Inc., for the U.S. Department of Energy's National Nuclear Security Administration under contract DE-NA0003525.

Revision Log

Revision	Date	Affected Pages	Revision Description
0	31 March 2020	All	Initial Release

Document pages that are:

Export Controlled:	None
IP/Proprietary/NDA Controlled:	None
Sensitive Controlled:	None
Unlimited:	All

Sandia National Laboratories is a multimission laboratory managed and operated by National Technology and Engineering Solutions of Sandia, LLC, a wholly owned subsidiary of Honeywell International Inc., for the U.S. Department of Energy's National Nuclear Security Administration under contract DE-NA0003525.

Executive Summary

In 2010, the U.S. Department of Energy created its first Energy Innovation Hub, which is focused on developing high-fidelity and high-resolution modeling and simulation (M&S) tools for modeling of light water reactors (LWRs). This hub, the Consortium for Advanced Simulation of LWRs (CASL), has developed an LWR simulation tool called the Virtual Environment for Reactor Applications (VERA). The multi-physics capability of VERA is achieved through the coupling of single-physics codes, including CTF (the CASL version of Coolant Boiling in Rod Arrays–Three Field (COBRA-TF)), Michigan Parallel Characteristics Transport (MPACT), BISON, and Materials Performance and Optimization (MPO) Advanced Model for Boron Analysis (MAMBA).

As part of its M&S efforts, CASL has identified various challenge problems, including Crud Induced Power Shift (CIPS), Crud-Induced Localized Corrosion (CILC), Pellet-Cladding Interaction (PCI), and Departure from Nucleate Boiling (DNB). This work addresses CASL milestone L2:VVI.P19.03, which focuses on uncertainty quantification of crud, which is relevant to both CIPS and CILC. This is achieved through an analysis and separate effects validation of the thermal hydraulic phenomenon known as subcooled boiling.

As part of this work, various sources of experimental data are examined and compared to different options for empirical modeling of subcooled boiling. Through this analysis, a complete understanding of the underlying models and their implementation details are understood. A subset of these data are incorporated into a separate effects validation study of CTF. The Westinghouse Advanced Loop Tester (WALT) and Rohsenow experiments are modeled, and it is shown that the newly-implemented Gorenflo correlation is more accurate than the existing Chen and Thom correlations.

Table of Contents

List of Figures

List of Tables

List of Acronyms

AOA	Axial Offset Anomaly
CASL	Consortium for Advanced Simulation of LWRs
CE	Combustion Engineering
COBRA-TF	Coolant Boiling in Rod Arrays–Three Field
CTF	The CASL version of COBRA-TF
PCI	Pellet-Cladding Interaction
DNB	Departure from Nucleate Boiling
LWR	light water reactor
CILC	Crud-Induced Localized Corrosion
CIPS	Crud Induced Power Shift
M&S	modeling and simulation
MPO	Materials Performance and Optimization
MAMBA	MPO Advanced Model for Boron Analysis
MPACT	Michigan Parallel Characteristics Transport
NESTOR	New Experimental Studies of Thermal-hydraulics of Rod bundles
NRC	Nuclear Regulatory Commission
PIRT	Phenomena Identification Ranking Table
PWR	pressurized water reactor
RMSE	root mean square error
SNL	Sandia National Laboratories
TRACE	The TRAC/RELAP Advanced Computational Engine
VERA	Virtual Environment for Reactor Applications
WALT	Westinghouse Advanced Loop Tester

1. Introduction

In light water reactors (LWRs), the steam generator and structural materials are gradually corroded over time. These corrosion products—mostly iron, nickle, and chromium oxides—are transported by the reactor coolant and preferentially deposit on the outer surface of nuclear fuel rods. These deposits were identified in LWRs as early as 1944 and were colloquially called "crud". In 1959, this colloquial term was formed into the backronym Chalk River Unidentified Deposits (CRUD) by Commander E. E. Kinter, who oversaw the analysis of crud deposits at the Chalk River site [1].

Crud deposition has important effects on reactor operation that motivate the development of high-fidelity and high-resolution modeling and simulation (M&S) tools. As a result, the Consortium for Advanced Simulation of LWRs (CASL) has focused development on two crud-specific challenge problems: Crud-Induced Localized Corrosion (CILC) and Crud Induced Power Shift (CIPS). This work focuses on preliminary qualification and validation of CIPS.

CIPS—previously known as Axial Offset Anomaly (AOA)—is a process whereby boron deposits in the crud affect the reactor power distribution. Crud accumulation is exacerbated in areas affected by subcooled boiling, since impurities are left behind when bubbles form [2]. In pressurized water reactors (PWRs), crud deposits are concentrated in the upper core region, since the bulk fluid temperature is sufficiently high that subcooled boiling is possible. As crud grows on the surface of nuclear fuel rods, this porous material can accumulate lithium borate. Therefore, the boron deposits suppress the neutron flux towards the top of the reactor core as neutrons are absorbed; the power shape is *shifted* towards the bottom of the core.

Nuclear power plants affected by CIPS must run at reduced power or shut down. For example, the Callaway plant in Missouri experienced significant CIPS in 1997. The accumulation of lithium borate in the crud caused a -15% axial offset, which led the operators to reduce reactor power to 70%. This significantly reduced the power output of the reactor, which reduces the economic benefit of the plant. This demonstrates the large impact of CIPS on reactor operation: it degrades the shutdown margin and decreases operational flexibility, particularly during reactor transients. Due to the effects of the large axial offset at the Callaway plant—which was the largest ever observed—the Nuclear Regulatory Commission (NRC) released an information notice [3] and industry leaders released operational guidelines to avoid crud buildup [4].

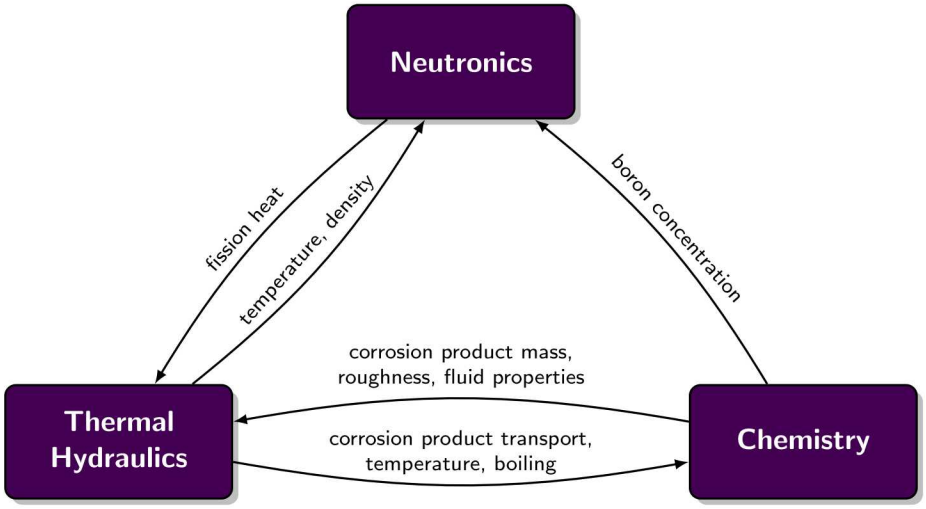

Figure 1.1: Nonlinear Feedback

The deposition of crud is a complex multi-physics phenomena. Accurate modeling activities require a thorough understanding of corrosion, corrosion product transport and deposition, coolant boiling and chemistry, neutronics, and heat transfer characteristics of the crud. In addition, it is important to model the nonlinear coupling between each of these physics, which are shown in Figure 1.1. Each separate physical process impacts the others in complex nonlinear ways. Therefore, the modeling of crud has been a common research topic in the M&S community [5, 6, 7, 8].

Crud buildup is extremely sensitive to boiling [2]. As steam is formed, solid particles are left behind; therefore, corrosion products preferentially deposit during the boiling process. The flow boiling curve before dryout is shown in Figure 1.2. Before the onset of boiling, the flow is in the *single phase forced convection regime*. Boiling can take place at the surface of fuel rods when the bulk fluid temperature has not yet reached the saturation temperature, which is called *subcooled boiling*. Once the bulk fluid temperature has reached the saturation temperature, bubbles do not immediately condense after they are formed. This *saturated boiling* region is characterized by the bubbly, slug, and churn flow regimes. Traditionally, this process is modeled by defining a heat transfer correlation for the forced convection and saturated boiling regimes. The subcooled boiling regime is defined as an interpolation between the two correlations [9].

In PWRs, only subcooled boiling takes place at normal operating conditions. In fact, CASL Phenomena Identification Ranking Tables (PIRTs) have consistently ranked subcooled boiling as one of the most important phenomena determining crud buildup in PWRs [10, 11]. Therefore, this work focuses on analysis and validation of subcooled boiling models in the CASL version of Coolant Boiling in Rod Arrays–Three Field (COBRA-TF), which is called CTF. CTF is the thermal hydraulic tool in Virtual Environment for Reactor Applications (VERA).

Chapter 2 outlines the general process of subcooled boiling, correlations used to calculate the heat

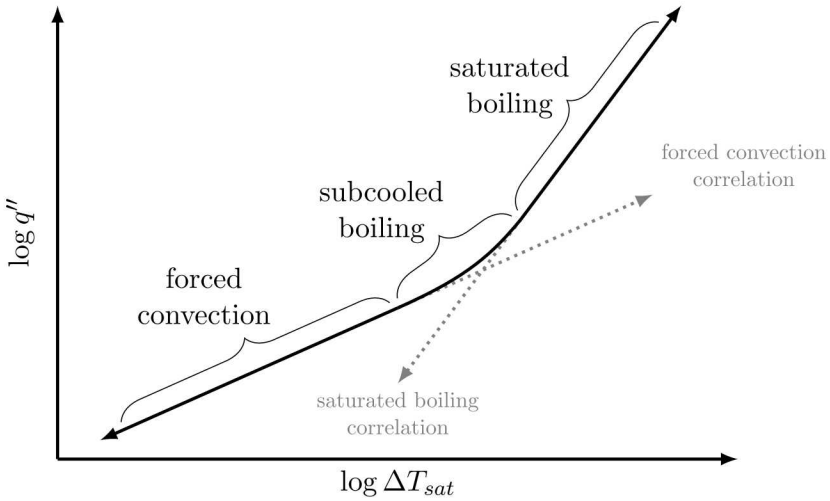

Figure 1.2: Pre-dryout flow boiling curve

transfer correlation, and compares these correlations to a variety of experimental data. Chapter 3 performs a separate effects validation study of subcooled boiling for CTF. A conclusion and discussion of future work are in Chapter 4.

2. Subcooled boiling

Subcooled boiling is chararacterized by the formation of small vapor bubbles at nucleation sites of a heated surface [12]. The water near the heated surface may be locally saturated, even though the bulk fluid is not. "Partial subcooled boiling" occurs before fully developed subcooled boiling, which has comparatively fewer nucleation sites and is characterized by a bubble vapor layer along the heated surface. These bubbles will generally collapse very soon after forming as the bulk fluid temperature is lower than the saturation temperature.

The bubble vapor layer will grow as the bulk fluid temperature increases. The bubbles in this vapor layer coalesce and collapse until eventually bubbles begin to detach from the heated surface wall [13]. As the bulk fluid temperature is too low to support the existence of the bubble, the detached bubbles will collapse downstream from their detachment point. In this region of fully developed subcooled boiling, there may be significant void in the flow, even though the bulk fluid is below the saturation temperature. The governing temperature difference in fully developed subcooled nucleate boiling is wall superheat ($T_w - T_{sat}$) rather than total temperature difference ($T_w - T_L$) [12].

Some of the models developed to approximate heat transfer in the subcooled boiling regime are described in Section 2.1.

2.1 Models

Four models for boiling heat transfer are described in this section: Chen [14], Thom [15], Gorenflo [16], and Gungor & Winterton [17]. In the case where CTF-specific modifications have been made to the model, these changes are summarized after the subheading "as implemented in CTF."

2.1.1 Chen

The Chen correlation covers the entire range of saturated boiling and expresses the two-phase heat transfer coefficient as the sum of the contributions due to forced convection and nucleate boiling [14]. It has since been modified to be applicable to subcooled boiling. See list below for nomenclature and units for the Chen correlation.

c_p =specific heat [btu/lbm/°F]
D =diameter [ft]
F =Reynolds number factor [−]
G =mass flux [lbm/hr/ft^2]
g_c =gravitational constant [1 lbf to lbmft/hr^2]
h =heat transfer coefficient [btu/ft^2/hr/°F]
k =thermal conductivity [btu/ft/hr/°F]
P =pressure [lbf/ft^2]
Pr =Prandtl number [−]
q'' =heat flux [btu/ft^2/hr]
Re =Reynolds number [−]
S =suppression factor [−]
T =temperature [°F]
x =weight fraction of vapor [−]
X_{tt} =Martinelli parameter [−]
ΔT =$T_w - T_{sat}$ = wall superheat [°F]
ΔP =difference in vapor pressure corresponding to ΔT [lbf/ft^2]
λ =latent heat of vaporization [btu/lbm]
μ =viscosity [lbm/ft/hr]
ν =$1/\rho$ = specific volume [ft^3/lbm]
ρ =density [lbm/ft^3]
σ =vapor-liquid surface tension [lbf/ft]

Subscripts

f =value for liquid
fc =forced convection
L =value for bulk
nb =nucleate boiling
sat =value at saturation
tp =two phase
v =value for vapor
w =value at wall

As Implemented by Chen The Chen correlation, as implemented originally in [14], was formulated using saturated boiling data at relatively low pressures (i.e. 6.9 MPa). It expresses the two-phase heat transfer coefficient, h_{tp}, as the sum of the heat transfer coefficients due to forced convection, h_{fc}, and nucleate boiling h_{nb}:

$$h_{tp} = h_{fc} + h_{nb}. \tag{2.1}$$

The forced convection term, h_{fc}, was written by Chen as a modified Dittus-Boelter [18] equation:

$$h_{fc} = 0.023 Re_L^{0.8} Pr_L^{0.4} (k_L/D) F \tag{2.2}$$

where F is related to the ratio of the two-phase Reynolds number, Re, and the liquid Reynolds number, Re_L:

$$Re_L = \frac{DG(1-x)}{\mu_L} \tag{2.3}$$

$$Re = Re_L F^{1.25} \tag{2.4}$$

F was assumed by Chen to be a function of the Martinelli parameter, X_{tt}, and was presented graphically by Chen based on experimental data [14]. Todreas and Kazimi [19] use the following approximation of F as a function of the Martinelli parameter, based on the graph in [14]:

$$F = \begin{cases} 1 & \text{if } \frac{1}{X_{tt}} < 0.1 \\ 2.35\left(0.213 + \frac{1}{X_{tt}}\right)^{0.736} & \text{if } \frac{1}{X_{tt}} > 0.1 \end{cases}, \tag{2.5}$$

where the Martinelli parameter is defined as:

$$X_{tt} = \left(\frac{1-x}{x}\right)^{0.9}\left(\frac{\rho_v}{\rho_f}\right)^{0.5}\left(\frac{\mu_f}{\mu_v}\right)^{0.1}. \tag{2.6}$$

Chen used the Forster-Zuber [20] equation as a basis for the formulation of the heat transfer coefficient due to nucleate boiling. The Forster-Zuber [20] equation was determined for pool boiling and used a mean effective superheat quantity since for pool boiling, the difference between this term and the wall superheat is small. However, Chen [14] noted that during convective boiling, the difference between these terms were not negligible and formulated the Forster-Zuber equation for h_{nb} as

$$h_{nb} = 0.00122\left(\frac{k_f^{0.79} c_{pf}^{0.45} \rho_f^{0.49} g_c^{0.25}}{\sigma^{0.5} \mu_f^{0.29} \lambda^{0.24} \rho_v^{0.24}}\right)(\Delta T)^{0.24}(\Delta P)^{0.75} S. \tag{2.7}$$

where $\Delta P = P(T_w) - P(T_{sat})$ and $\Delta T = T_w - T_{sat}$. The pressure at the wall temperature is $P(T_w)$ and the saturation pressure is $P(T_{sat})$. The constant g_c is a conversion factor necessary for British units (lbf to lbm $\cdot$ ft/hr^2).

The suppression factor, S, takes into account the difference between the mean effective superheat and the wall superheat. It approaches unity at high Reynolds numbers and zero at low Reynolds numbers. Chen presented S graphically as a function of Re in [14]. Todreas and Kazimi [19] use the following approximation of S as a function of the Re, based on the graph in [14]:

$$S = \frac{1}{1 + 2.53 \times 10^{-6} Re^{1.17}} \tag{2.8}$$

Chen then expresses h_{tp} as the sum of h_{fc} and h_{nb}, which can be used to find the heat flux, q_{tp}:

$$h_{tp} = h_{fc} + h_{nb}, \tag{2.9}$$

$$q''_{tp} = h_{tp}(T_w - T_{sat}). \tag{2.10}$$

Modifications for Subcooled Boiling Collier [12] discussed a modification to the Chen correlation for the subcooled boiling region. The modification assumes the total heat flux is the sum of the contributions due to single-phase forced convection and nucleate boiling.

$$q''_{tp} = h_{fc}(T_w - T_L) + h_{nb}(T_w - T_{sat}) \tag{2.11}$$

This modification sets F to unity, and S is calculated with quality $x = 0$.

As Implemented in CTF The Chen correlation, as implemented in CTF, has a few key differences from the Chen formulation [14].

The Reynolds number factor, F, is based off the graphical representation of $F(X_{tt})$ in [14] and is expressed in CTF as:

$$F = \begin{cases} 1 & \text{if } \frac{1}{X_{tt}} < 0.1 \\ 2.34\left(0.213 + \frac{1}{X_{tt}}\right)^{0.736} & \text{if } \frac{1}{X_{tt}} > 0.1 \end{cases}. \tag{2.12}$$

CTF uses Equation 2.7 from [14], however the CTF implementation uses a different approximation of suppression factor, S, from the graph in [14].

$$h_{nb} = 0.00122\left(\frac{k_f^{0.79} c_{pf}^{0.45} \rho_f^{0.49} g_c^{0.25}}{\sigma^{0.5} \mu_f^{0.29} \lambda^{0.24} \rho_v^{0.24}}\right)(\Delta T)^{0.24}(\Delta P_{CTF})^{0.75} S \tag{2.7}$$

The suppression factor in CTF was approximated from [14] as

$$S = \begin{cases} [1 + 0.12Re^{1.14}]^{-1} & \text{if } Re < 32.5 \\ [1 + 0.42Re^{0.78}]^{-1} & \text{if } 32.5 < Re < 50.9 \\ 0.1 & \text{if } Re > 50.9 \end{cases}. \tag{2.13}$$

where Re in Equation 2.4 is scaled by 10^{-4}.

$$Re = Re_L \times 10^{-4} F^{1.25} \tag{2.14}$$

In CTF, $\Delta P = P(T_w) - P(T_{sat})$ is approximated by

$$\Delta P_{CTF} = \left[\frac{5.4042\lambda}{\nu_{fv}(T_{sat} + 460)}\right](T_w - T_{sat})^A \tag{2.15}$$

where

$$A = \frac{1.0306}{(\log_{10} P)^{0.017}} + \frac{0.0020632}{(\log_{10} P)^{1.087}} \max[0.0, (T_w - T_{sat} - 5.0)], \tag{2.16}$$

$$\nu_{fv} = \frac{1}{\rho_v} - \frac{1}{\rho_f}. \tag{2.17}$$

The origin of this approximation is unclear. The two-phase heat transfer coefficient and heat flux are calculated according to Equation 2.9 and Equation 2.10:

For subcooled boiling, CTF uses the modifications expressed by Collier [12] in Equation 2.11. The modification also sets F to unity, and S is calculated with quality $x = 0$.

2.1.2 Thom

The Thom correlation was formulated for conventional heat transfer without boiling and for subcooled nucleate boiling [15]. In the formulation used by Thom, the correlation is insensitive to flow rate or flow quality but is highly sensitive to pressure. See list below for nomenclature and units for the Thom correlation.

c_p =specific heat [btu/lbm/°F]
D =diameter [ft]
G =mass flux [lbm/hr/ft^2]
h =heat transfer coefficient [btu/ft^2/hr/°F]
k =thermal conductivity [btu/ft/hr/°F]
P =pressure [psi]
Pr =Prandtl number [−]
q'' =heat flux [btu/ft^2/hr]
Re =Reynolds number [−]
T =temperature [°F]
ΔT_{sat} =$T_w - T_{sat}$ = wall superheat [°F]
μ =viscosity [lbm/ft/hr]

Subscripts

fc =forced convection
L =value for bulk
nb =nucleate boiling
sat =value at saturation
tp =two phase
w =value at wall

As Implemented by Thom The Thom correlation was written for non-boiling and subcooled boiling regions. Because the experimental data was in steady state, the correlation was written with the assumption that heat flux was known. However, quantities such as heat transfer coefficient and the wall superheat are unknown in CTF. The Thom correlation was fitted against data with the following approximate operating conditions ranges: pressure 5.2 MPa to 13.8 MPa, mass flux 1040 kg/s/m^2 to 3800 kg/s/m^2, and heat flux 0 kW/m^2 to 1600 kW/m^2.

The Thom correlation [15] uses a modified Dittus-Boelter equation to determine the non-boiling heat transfer coefficient. This change was made to better match the data used by Thom at lower mass flow rates.

$$h = 0.134 Re^{0.65} Pr^{0.4} \left(\frac{k}{D}\right) = 0.134 \left(\frac{c_{pL} G^{0.65}}{(D/\mu_L)^{0.35} Pr_L^{0.6}}\right) \tag{2.18}$$

In the subcooled boiling region, Thom [15] observed that values of $q/(Tw - T_L)$ were strongly dependent on the heat flux, but insensitive to flow rate and he used the following formulation to approximate q''/h:

$$\frac{q''}{h} = T_{sat} + \Delta T_{sat} - T_L. \tag{2.19}$$

The ΔT_{sat} term was formulated as a modified Jens-Lottes [21] equation. ΔT_{sat} is dependent on only heat flux and system pressure:

$$\Delta T_{sat} = \frac{0.072 q''^{0.5}}{e^{(P/1260)}}. \tag{2.20}$$

Equation 2.19 can then be rewritten in terms of q''_{tp}.

$$q''_{tp} = h(T_{sat} + \Delta T_{sat} - T_L) \tag{2.21}$$

As Implemented in CTF The CTF formulation of the Thom correlation uses an unmodified Dittus-Boelter equation to determine the forced convection heat transfer coefficient:

$$h_{fc} = 0.023 Re_L^{0.8} Pr_L^{0.4} (k_L/D). \tag{2.22}$$

In CTF, the Thom correlation was formulated to determine q''_{nb} from a known wall superheat. This is different from Thom [15], who assumed that wall superheat was an unknown quantity. Therefore, solving Equation 2.20 for heat flux determines the implementation in CTF:

$$q''_{nb} = \frac{e^{2P/1260}}{0.072^2} (T_w - T_{sat})^2 \tag{2.23}$$

The CTF formulation from the Thom correlation notably differs in how the q''_{tp} is determined. Whereas the Thom correlation uses Equation 2.21 to determine the two-phase heat flux, CTF uses an additive approach of contributions due to forced convection and boiling.

$$q''_{tp} = h_{fc}(T_w - T_L) + q''_{nb} \tag{2.24}$$

2.1.3 Gungor and Winterton

Gungor & Winterton [17] proposed a correlation to give an overall heat transfer coefficient that accounts for both nucleate boiling and forced convection heat transfer components. This approach is similar to the Chen correlation, but with a dependence on the boiling number. The Gungor & Winterton correlation was tested against both subcooled and saturated boiling data for vertical and horizontal flow. See list below for nomenclature and units for the Gungor & Winterton correlation.

Bo =boiling number [−]
c_p =specific heat [J/kg/°C]
D =diameter [m]
E =enchancement factor [−]
Fr =Froude number[−]
G =mass flux [kg/s/m^2]
h =heat transfer coefficient [W/m^2/°C]
k =thermal conductivity [W/m/°C]
M =molecular weight [g/mol]
P =pressure [N/m^2]
P_r =P/P_{crit} = reduced pressure [−]
Pr =Prandtl number [−]
q'' =heat flux [W/m^2]
Re =Reynolds number [−]
S =suppression factor [−]
T =temperature [°C]
x =weight fraction of vapor [−]
X_{tt} =Martinelli parameter [−]
λ =latent heat of vaporization [J/kg]
μ =viscosity [Ns/m^2]
ρ =density [kg/m^3]
σ =vapor-liquid surface tension [N/m]

Subscripts

fc =forced convection
L =value for bulk
$pool$ =pool boiling

sat =value at saturation
w =value at wall
tp =two phase

The Gungor & Winterton correlation uses the same approach as Chen which accounts for two contributions to the heat transfer coefficient: nucleate boiling and forced convection. Like other correlations noted, the forced convection heat transfer coefficient, h_l is given by the Dittus-Boelter equation.

$$h_{tp} = Eh_{fc} + Sh_{pool} \tag{2.25}$$

$$h_{fc} = 0.023 Re_L^{0.8} Pr_L^{0.4} (k_L/D) \tag{2.26}$$

The enhancement factor, E, takes into account the higher velocities and forced convection heat transfer in two-phase flow compared to single-phase flow. The Gungor-Winterton enhancement factor is a function of the Martinelli parameter and the boiling number, Bo. The boiling number is a dimensionless parameter quantifying the disturbance of the boundary layer next to the heat transfer surface due to the generation of vapor.

$$E = 1 + 24000 Bo^{1.16} + 1.37 X_{tt}^{-0.86} \tag{2.27}$$

$$Bo = \frac{q''}{\lambda G} \tag{2.28}$$

The pool boiling term, h_{pool} is multiplied by a suppression factor, S. The suppression factor takes into account that the boundary layer will be thinner due to forced convection and it is a function of the two-phase Reynolds number. In this equation, P_r is the reduced pressure.

$$h_{pool} = 55 P_r^{0.12} (-\log_{10} P_r)^{-0.55} M^{-0.5} q''^{0.67} \tag{2.29}$$

$$S = \frac{1}{1 + 1.15 \times 10^{-6} E^2 Re_L^{1.17}} \tag{2.30}$$

$$P_r = P/P_{crit} \tag{2.31}$$

It should be noted that in this correlation, it is assumed that the heat flux q'' is a known quantity since the data is in steady state.

Modifications for Subcooled Boiling In the case of subcooled boiling, the enhancement factor is equal to unity as there is little net vapor generation. The equation for subcooled boiling is

$$q_{tp} = h_{fc}(T_w - T_L) + Sh_{pool}(T_w - T_{sat}). \tag{2.32}$$

2.1.4 Gorenflo

Gorenflo implemented a method of determining the pool boiling heat transfer coefficient based off a reference heat transfer coefficient at various operating conditions [16]. This model was implemented in The TRAC/RELAP Advanced Computational Engine (TRACE) for subcooled pool boiling and was incorporated into CTF for subcooled flow boiling. See list below for nomenclature and units for the Gorenflo correlation.

F_{PF} =pressure correction factor [−]
h =heat transfer coefficient [W/m^2/°C]
h_o =reference heat transfer coefficient [W/m^2/°C]
P_r =P/P_{crit} = reduced pressure [−]
q'' =heat flux [W/m^2]
q_o'' =reference heat flux [20 000 W/m^2]
R_p =surface roughness [µm]
R_{po} =reference surface roughness [µm]
T =temperature [°C]

Subscripts

bi =value at onset of nucleate boiling
fc =forced convection
L =value for bulk
pb =pool boiling
sat =value at saturation
tp =two phase
w =value at wall

As Implemented by Gorenflo Gorenflo [16] formulated an equation for the nucleate pool boiling heat transfer coefficient, h, based off a reference heat transfer coefficient, h_o. The value of h_o varies per fluid, but for water is equal to 5600 W/m^2/°C.

$$h = h_o F_{PF} (q''/q_o'')^n (R_p/R_{po})^{0.133} \tag{2.33}$$

In Equation 2.33, q_o'' is 20 000 W/m^2 and R_{po} is a reference surface roughness $R_{po} = 0.4$ µm. R_p is the surface roughness of the actual surface, which has a default value of 0.4 µm. F_{PF} and n are both functions of the reduced pressure, $P_r = P/P_{crit}$. For water, P_{crit} is equal to 220.64 bar. The equations for F_{PF} and n are:

$$F_{PF} = 1.73 P_r^{0.27} + \left(6.1 + \frac{0.68}{1 - P_r}\right) P_r^2, \text{ and} \tag{2.34}$$

$$n = 0.9 - 0.3 P_r^{0.15}. \tag{2.35}$$

It should be noted that these equations are for water, and other equations for F_{PF} and n are used for other fluids.

As Implemented in CTF The Gorenflo model, as implemented in CTF, uses the previous equations for F_{PF} (Equation 2.34) and n (Equation 2.35). The pool boiling heat transfer is defined as the following explicit expression:

$$q''_{pb} = \left(\frac{h_o F_{PF} (T_w - T_{sat})}{q''^n_o} \right)^{1/(1-n)} . \tag{2.36}$$

CTF uses a superposition of the forced convection heat flux and the pool boiling heat flux to obtain the two-phase boiling heat flux:

$$q''_{tp} = \left(q''^{\,3}_{fc} + (q''_{pb} - q''_{bi})^3 \right)^{(1/3)} \tag{2.37}$$

where q_{bi} is the pool boiling heat flux from Equation 2.36 calculated using the wall temperature at the onset of nucleate boiling for T_w.

2.2 Experimental Data

Several data sources were used to compare the different correlations. These data sources are summarized briefly below.

Sani Chen [14] used boiling data from several sources to create his correlation. The data from the Chen paper used for data comparisons in this report was collected by Sani (1960) [22]. Sani measured local heat transfer coefficients for nonboiling and boiling flow conditions in an electrically heated 304 stainless tube with an inner diameter of 18.27 mm. A summary of the boundary conditions employed by Sani are in Table 2.1.

Table 2.1: Sani (1960) [22] data summary

Parameter, Unit	Minimum	Maximum
Pressure, MPa	0.1099	0.2057
Mass Flux, kg/s/m^2	249.5	1036
Heat Flux, kW/m^2	42.9	157
Quality, %	0.77	14.3
Diameter, mm	18.27	18.27

Rohsenow A technical report with heat transfer and pressure drop data for a series of high heat flux experiments in water during non-boiling and subcooled boiling conditions [23]. Local heat transfer coefficients were measured for water flowing through a nickel tube with an inner diameter

of 4.57 mm. This set of data is explained in more detail in Chapter 3. A summary of the boundary conditions employed by Rohsenow are in Table 2.2.

Table 2.2: Rohsenow (1951) [23] data summary

Parameter, Unit	Minimum	Maximum
Pressure, MPa	10.3	13.8
Mass Flux, kg/s/m^2	2641	8046
Heat Flux, kW/m^2	2830	11000
Quality, %	0.0	0.0 (subcooled)
Diameter, mm	4.57	4.57

Rohsenow Book In his book, Rohsenow published two figures (9.5 and 9.6) showing the results of subcooled boiling [24, 9]. Both of these experiments were performed at atmospheric pressure and used a 2.39 mm diameter tube. These experiments varied mass velocity and pressure and recorded heat flux and wall superheat. A summary of the operating conditions employed by Rohsenow in these book figures is in Table 2.3.

Table 2.3: Rohsenow book (1961) [24, 9] data summary

Parameter, Unit	Minimum	Maximum
Pressure, MPa	0.101	0.101
Mass Flux, kg/s/m^2	16.4	64.7
Heat Flux, kW/m^2	2775	21200
Quality, %	0.0	0.0 (subcooled)
Diameter, mm	2.39	2.39

Stone Data was taken at the NASA Lewis Research Center and measured inner wall temperature distributions for numerous non-boiling and subcooled boiling flow conditions at low pressures [25]. The experiments used 5.84 mm and 12.19 mm inner diameter tubes with vertical flow of water and a uniform heat flux applied. Tables I, II, V, and VII from Stone were used for comparison. A summary of the operating conditions employed by Stone are in Table 2.4.

2.3 Analysis of Data

The data summarized in Section 2.2 was used to evaluate all correlations introduced in Section 2.1 to predict heat flux with a stand-alone Python script. The predicted values were then compared

Table 2.4: Stone (1971) [25] data summary

Parameter, Unit	Minimum	Maximum
Pressure, MPa	0.025	0.703
Mass Flux, kg/s/m^2	0.67	141.2
Heat Flux, kW/m^2	44.0	11400
Quality, %	0.0	70.0
Diameter, mm	5.84	12.19

to the experimental values. The results of this exercise are summarized in this section.

Figures 2.1, 2.2, 2.3, 2.4, and 2.5 show the measured heat flux versus the calculated heat flux per data set. The colors indicate which dataset the point belongs to and the marker type indicates the model used (see figure legend). Where CTF specific modifications were made to the model, that is indicated by a "(CTF)" in the figure legend next to the marker type.

Figures 2.6, 2.7, 2.8, 2.9, 2.10, and 2.11 show the calculated heat flux versus measured heat flux per correlation, using all data sets. In these figures, the colors indicate which dataset the point belongs to. This data is the same as shown in Figures 2.1, 2.2, 2.3, 2.4, and 2.5 in an easier to view format.

In general, most correlations tended to underpredict the heat flux, which is shown in the plots of calculated heat flux versus measured heat flux. Most correlations also more accurately predict the heat flux for the high heat flux datasets, specifically all Rohsenow data. However, the Stone data includes higher heat flux experiments and do not follow the same trend. Therefore, the observed accuracy at higher heat fluxes might be related to the experimental uncertainty or some other bias rather than an inherent characteristic of the correlations themselves. The notable exception to this is the Gorenflo correlation, which overpredicted some of the higher heat flux datapoints, sometimes by an entire order of magnitude. This can be seen in Figure 2.11. Figure 2.12 shows the Gorenflo correlation residual heat flux, $q_{model} - q_{exp}$, plotted against experiment superheat. As superheat increases, Gorenflo is less accurate. This is likely due to the CTF implimentation of Gorenflo which uses Equation 2.36 to calculate the pool boiling heat flux and raises superheat to an exponential power.

Tables 2.5 and 2.6 show tabulated validation metrics per correlation and data set. The validation metrics used were the mean of the residuals and root mean square error (RMSE). The equations for these two metrics can be found in the introduction of Chapter 3. The mean residual table shows that the overall residuals (row "All Data") of heat flux per correlation is negative for all correlations except Gorenflo. This confirms what was seen through visual inspection of the calculated heat flux versus measured heat flux plots; the correlations usually underpredicted the heat flux.

Table 2.6 shows that for the datasets used, the CTF implementation of the Chen correlation is

slightly less accurate than the Chen correlation as implemented by Chen. However, the modifications made in CTF for the Thom correlation do significantly improve the correlation accuracy over the Thom correlation as implemented by Thom and overall has the lowest RMSE value. Thom, as originally implemented, uses a modified Dittus-Boelter equation and does not express the total heat flux as the sum of the forced convection and nucleate boiling components. The Gungor and Winterton correlation has about the same accuracy as the unmodified Thom correlation. The Gorenflo correlation performs the worst overall out of all correlations. The worst RMSEs in the table are mostly attributed to the higher superheat value datapoints which resulted in extremely large residuals; other datasets have much lower residuals and RMSE values.

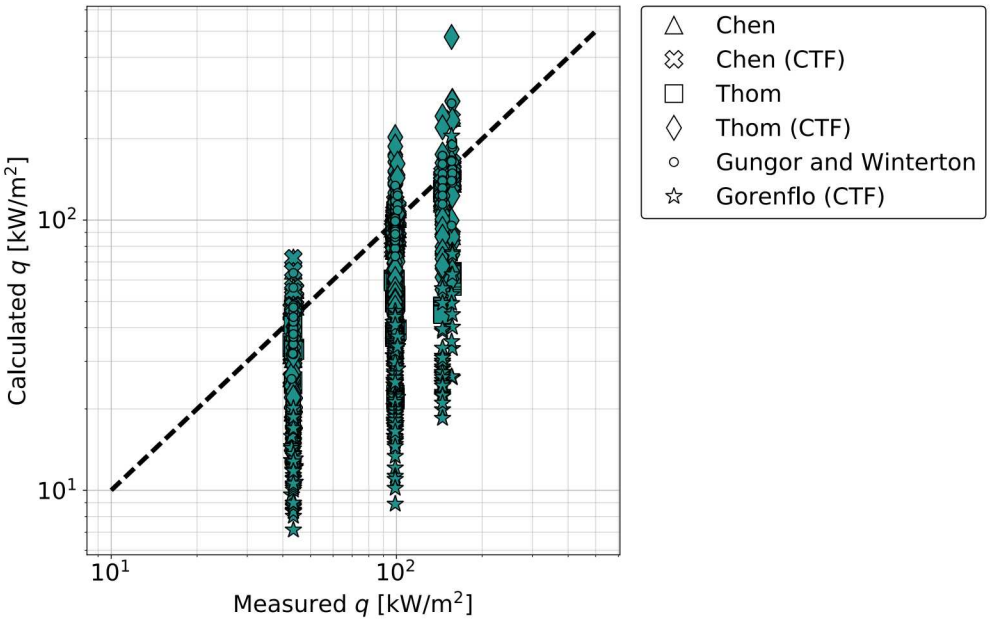

Figure 2.1: Sani (1960) [22] data showing measured heat flux versus calculated heat flux

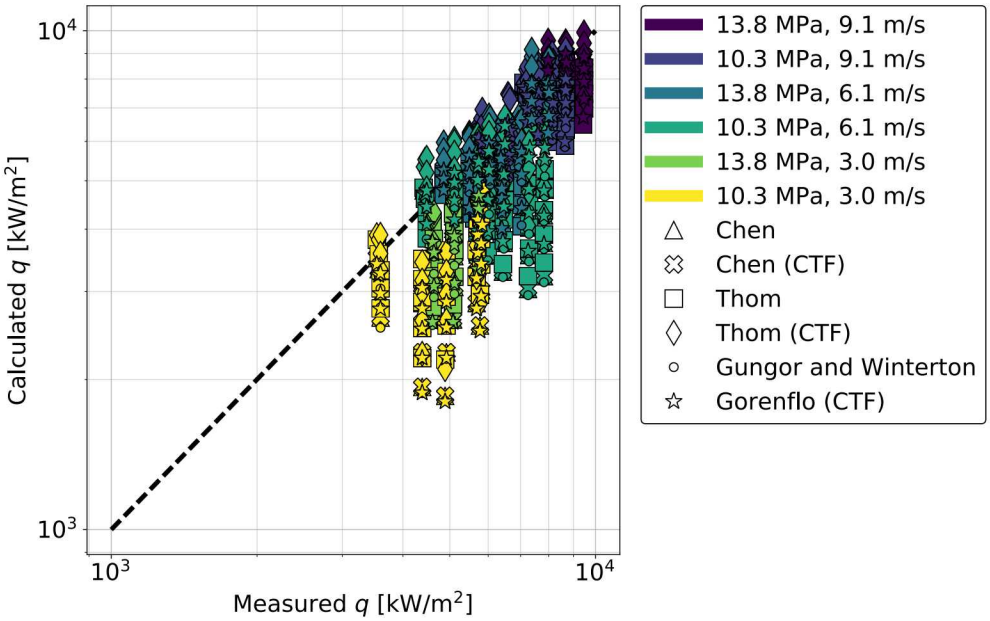

Figure 2.2: Rohsenow (1951) [23] data showing measured heat flux versus calculated heat flux

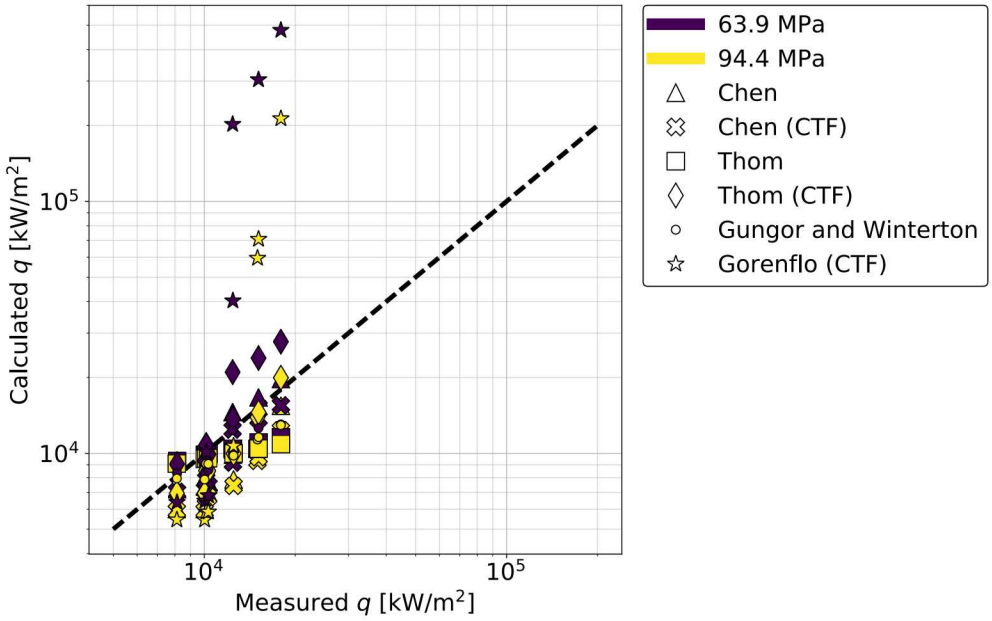

Figure 2.3: Rohsenow's book (1961) [24, 9], Figure 9.5 data showing measured heat flux versus calculated heat flux

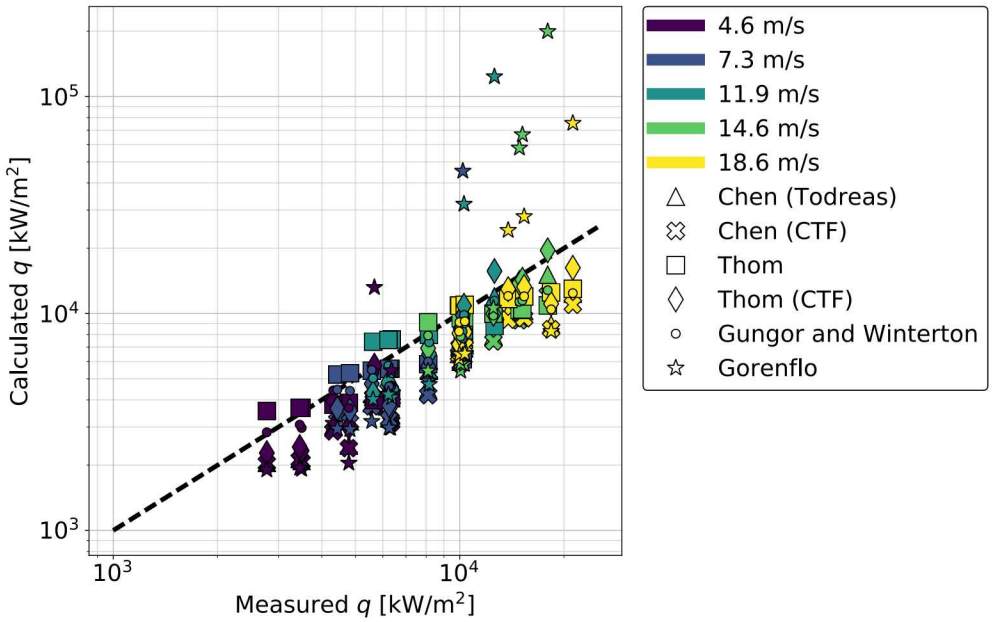

Figure 2.4: Rohsenow's book (1961) [24, 9], Figure 9.6 data showing measured heat flux versus calculated heat flux

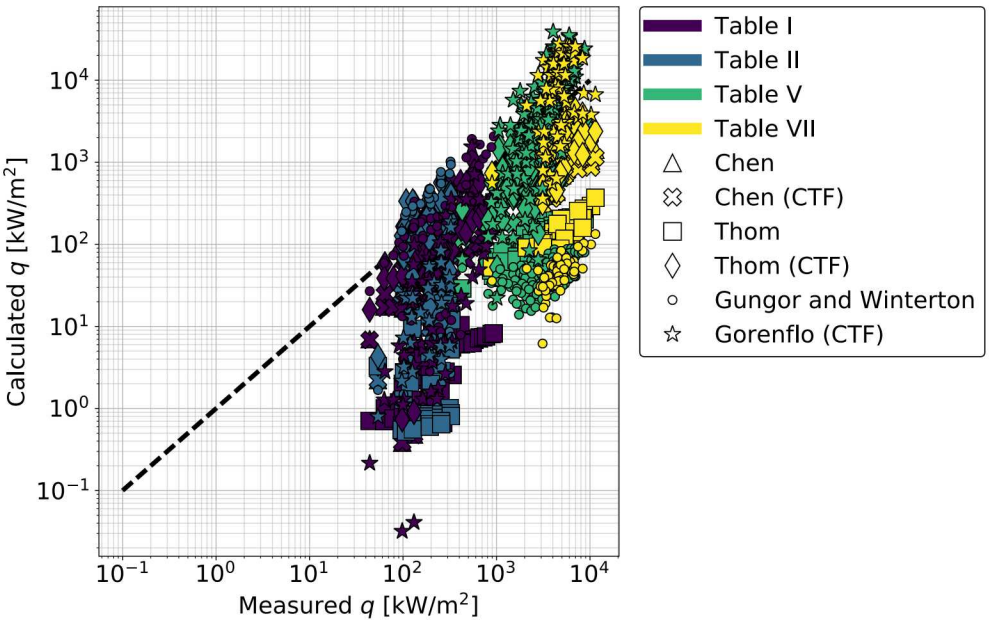

Figure 2.5: Stone (1971) [25] data showing measured heat flux versus calculated heat flux

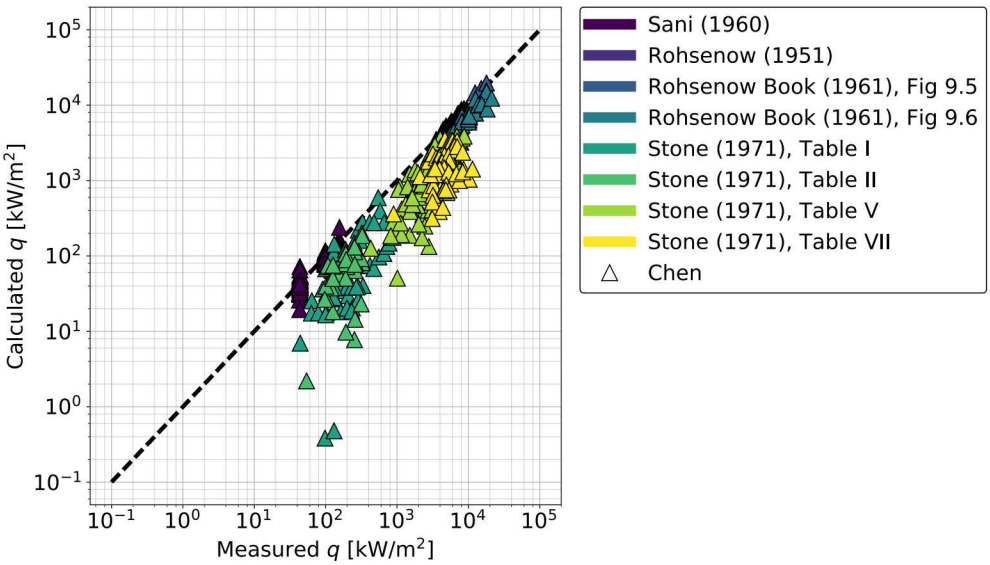

Figure 2.6: Measured heat flux versus calculated heat flux, using the Chen correlation

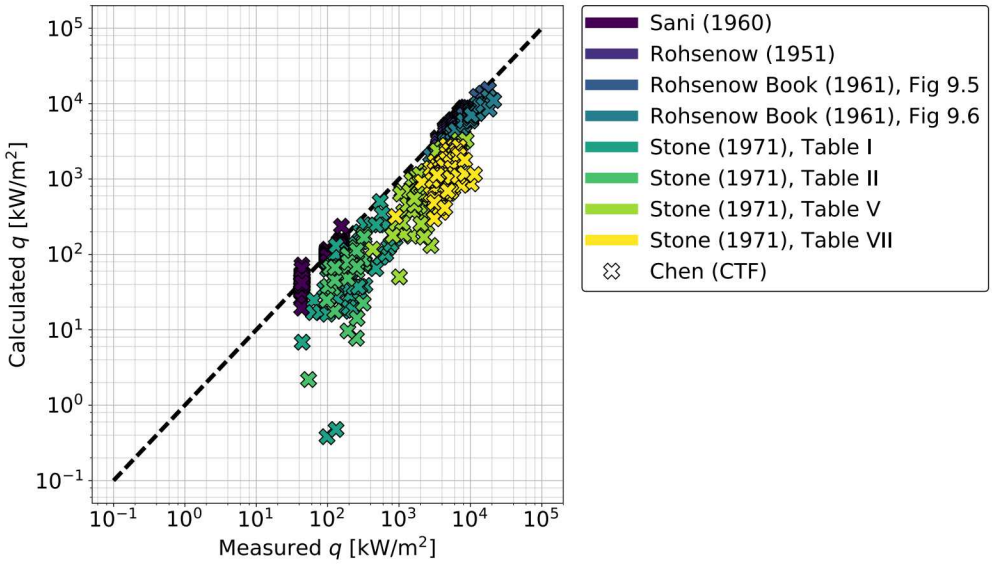

Figure 2.7: Measured heat flux versus calculated heat flux, using the Chen correlation

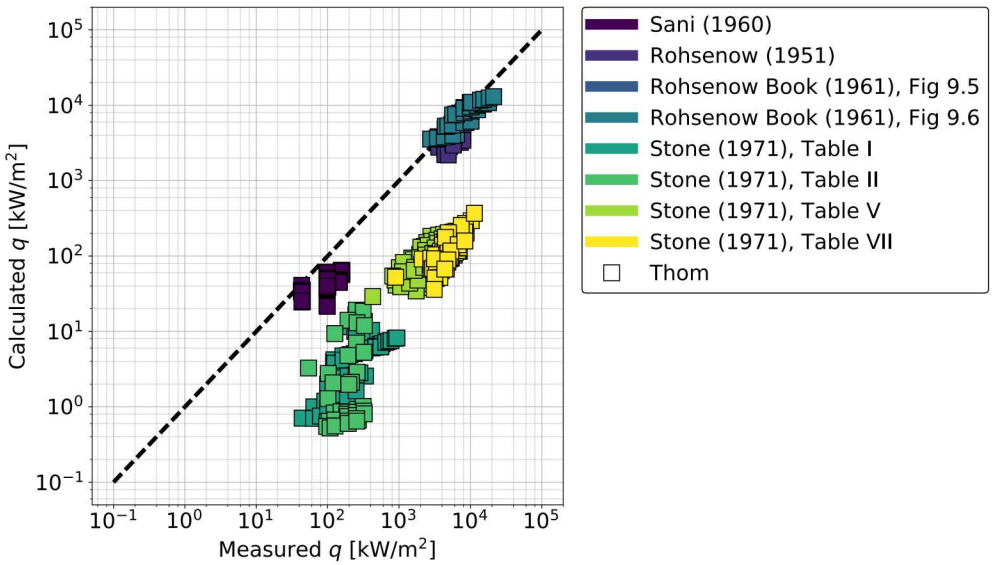

Figure 2.8: Measured heat flux versus calculated heat flux, using the Thom correlation

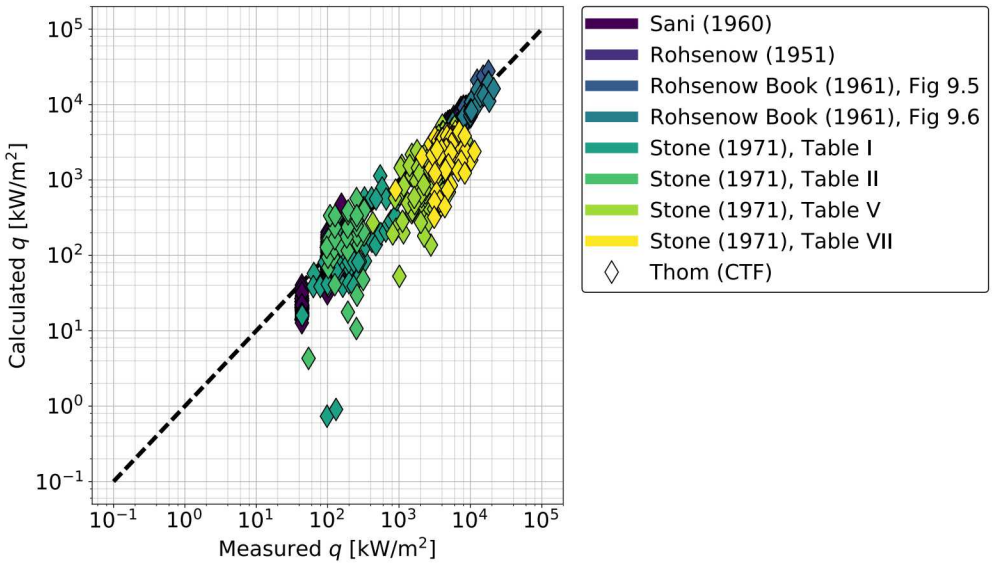

Figure 2.9: Measured heat flux versus calculated heat flux, using the Thom correlation, as implemented in CTF

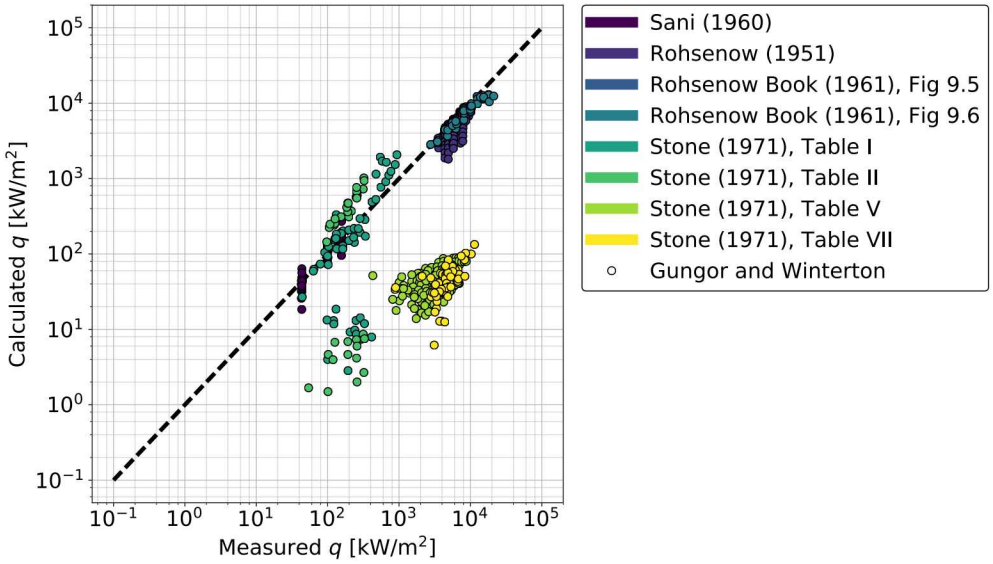

Figure 2.10: Measured heat flux versus calculated heat flux, using the Gungor and Winterton correlation

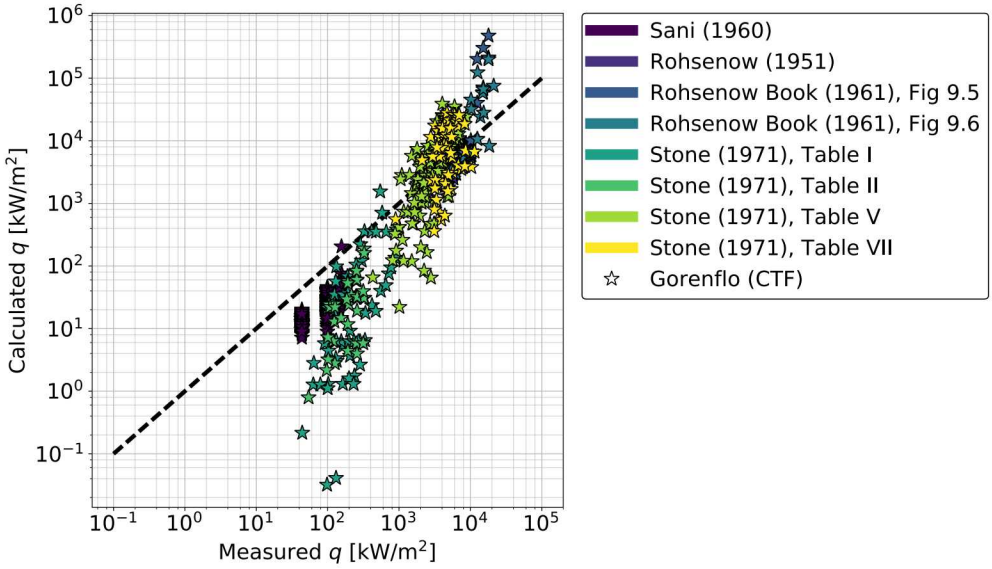

Figure 2.11: Measured heat flux versus calculated heat flux, using the Gorenflo correlation, as implemented in CTF

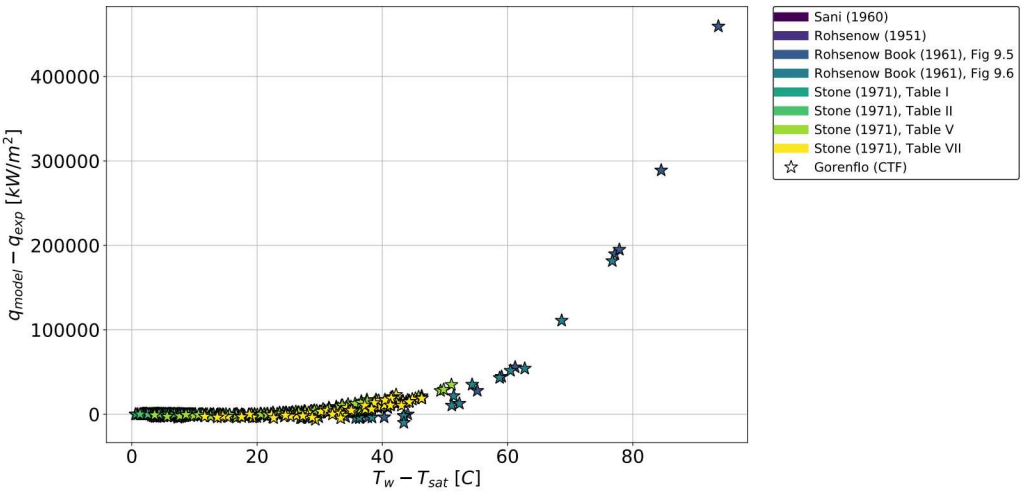

Figure 2.12: Residual heat flux as a function of the superheat, using the Gorenflo correlation, as implemented in CTF

Table 2.5: Mean residuals of $q_{model} - q_{exp}$ summary [kW/m^2]

Year	Author	Section	Chen		Thom		Gungor &	Gorenflo
			[14]	CTF	[15]	CTF	Winterton	CTF
1951	Rohsenow		-1260.6	-1254.6	-1282.0	-361.5	-1329.8	-1113.8
1960	Sani		-4.8	-5.0	-51.8	-24.7	-3.2	-69.2
1961	Rohsenow	Fig. 9.5	-2098.4	-3206.9	-2106.7	1191.8	-2106.6	77155.0
		Fig. 9.6	-3024.8	-3472.5	-1417.0	-1517.2	-1778.0	12556.8
1971	Stone	Tab. I	-176.3	-185.1	-271.0	-70.7	92.5	-180.5
		Tab. II	-129.3	-135.2	-197.7	-4.5	92.0	-168.0
		Tab. V	-2194.5	-2429.3	-3554.6	-1857.5	-3616.7	3626.0
		Tab. VII	-3179.2	-3557.9	-4823.6	-2323.9	-4892.9	6683.7
ALL DATA			-1214.3	-1351.3	-1678.2	-767.6	-1659.0	3256.4

Table 2.6: RMSE of $q_{model} - q_{exp}$ summary [kW/m^2]

Year	Author	Section	Chen		Thom		Gungor &	Gorenflo
			[14]	CTF	[15]	CTF	Winterton	CTF
1951	Rohsenow		1652.6	1647.8	1617.6	1159.5	1716.5	1496.4
1960	Sani		12.5	12.5	59.1	47.7	14.2	75.0
1961	Rohsenow	Fig. 9.5	2976.0	3592.6	3233.9	4176.8	2607.2	153001.2
		Fig. 9.6	3552.8	4057.0	2798.5	2248.6	2663.5	39105.0
1971	Stone	Tab. I	241.4	248.5	339.6	202.3	362.3	291.1
		Tab. II	145.5	150.5	211.8	128.3	284.2	181.8
		Tab. V	2423.2	2668.6	3892.9	2237.4	3957.5	6975.3
		Tab. VII	3585.7	3910.6	5107.8	2946.8	5183.4	10444.7
ALL DATA			1952.6	2146.5	2689.5	1688.1	2713	23129.1

3. Separate Effects Validation

CTF has been validated using two integral effects facilities that include subcooled boiling [26]: the Combustion Engineering (CE) facility at Columbia University [27], and the New Experimental Studies of Thermal-hydraulics of Rod bundles (NESTOR) facility in France [28]. Both of these facilities model prototypical PWR geometry and operating conditions. Therefore, these facilities include various physics effects besides subcooled boiling, including spacer grid effects and geometry changes. Therefore, this chapter focuses on separate effects validation of the CTF subcooled boiling model. Separate effects validation is an important part of the validation process because it ensures that compensating errors between physics models are minimized [29].

Both of the experimental facilities in this work consist of steady state flow through a short tube. For this case, the validation process is relatively simple. Convective heat transfer is essentially governed by the equation $q'' = hA(T_f - T_w)$. Assuming that external energy losses are negligible, the temperature rise in the fluid can be found via an energy balance, since it is in steady state and the heat generation in the solid is fixed. Therefore, the heat flux q'', surface area A, and fluid temperature T_f are essentially fixed. So the interaction between the wall temperature T_w and the heat transfer coefficient h is of primary interest. Since the heat transfer coefficient cannot be directly measured, the wall temperature becomes the quantity of interest for the validation process.

Separated effects validation is performed for the Rohsenow experiments in Section 3.1 and for the WALT facility in Section 3.2. To quantify the results, three validation metrics are defined to measure the overall bias, data spread, and total distance: the mean of the residuals, standard deviation of the residuals, and RMSE:

mean
$$\mu = \frac{1}{N}\sum_{i=1}^{N}\left(T_{w,CTF} - T_{w,exp}\right), \tag{3.1}$$

standard deviation
$$\sigma = \sqrt{\frac{1}{N}\sum_{i=1}^{N}\left(T_{w,CTF} - T_{w,exp} - \mu\right)^2}, \tag{3.2}$$

RMSE
$$\sqrt{\frac{1}{N}\sum_{i=1}^{N}\left(T_{w,CTF} - T_{w,exp}\right)^2}. \tag{3.3}$$

3.1 Rohsenow

In 1951, Rohsenow published the results of a subcooled boiling experiment [23]. He executed his tests using a 0.1805 in diameter nickel tube with a length of 9.4 in. A copper shield surrounded the tube and was used to heat it. Thermocouples measured the temperature at seven axial locations on the outside of the shield, though the first and last axial locations are not reported due to entrance and exit effects. Rohsenow estimated the inside tube temperature from the thermocouple measurements using a Taylor series, resulting in an estimated error bound of $\pm 3^{\circ}$F.

Distilled and degassed water was passed through the heated tube. Inlet and outlet coolant temperatures were measured and pressure was measured at the inlet. Steady state measurements were taken at two pressures, three mass fluxes, and a variety of heat fluxes. Therefore, each experiment measured four axial locations in the tube which all had similar conditions but different liquid subcooling. Rohsenow used these results to create a variety of plots and conclusions, which were later incorporated into textbooks [9, 30].

This facility is modeled in CTF using a single rod-centered channel with twenty axial nodes. The flow area, wetted perimeter, and rod surface area are set consistent with the tube geometry of the Rohsenow experiment. Rohsenow did not report actual pressure measurements, so the reported approximate pressure is set to the outlet pressure boundary condition. The inlet boundary conditions are determined from the experimentally reported inlet temperature and mass flux. For each run, the exit fluid temperature is extracted from the CTF output and compared to the experimentally measured value (to ensure a consistent energy balance). In addition, the entire wall temperature distribution is extracted from the output. Linear interpolation is used to approximate the wall temperature at each thermocouple location, which are compared to the experimentally reported values. Initial analysis was performed to show that the interpolation results in a maximum error $\pm 0.05^{\circ}$C, which is well within experimental uncertainty.

The difference between CTF and experimentally reported wall temperatures are shown in Figure 3.1. The colors indicate which experiment is being represented (see Appendix A for the experimental conditions, measurements, and results for each individual experiment). Three different options—indicated by marker shape in the figure—are analyzed: Chen, Thom, and Gorenflo. Note that the Gorenflo model also uses the new CTF model for the onset of nucleate boiling. In general, the Chen correlation leads to large over-predictions of the wall superheat. Thom predictions are closer, and the Gorenflo correlation is the most accurate; however, some experiments do not converge when using the Gorenflo correlation. In addition, all correlations are less accurate at higher axial locations, which indicates that the accuracy decreases with decreased fluid subcooling.

Each of the three validation metrics are shown in Table 3.1 for each choice of correlation: Chen, Thom, and Gorenflo. As observed in Figure 3.1, the Chen correlation is significantly less accurate than the other models and Gorenflo is slightly more accurate than Thom. The three metrics are shown in Table 3.2 as a function of the axial location at which the measurement was taken. The

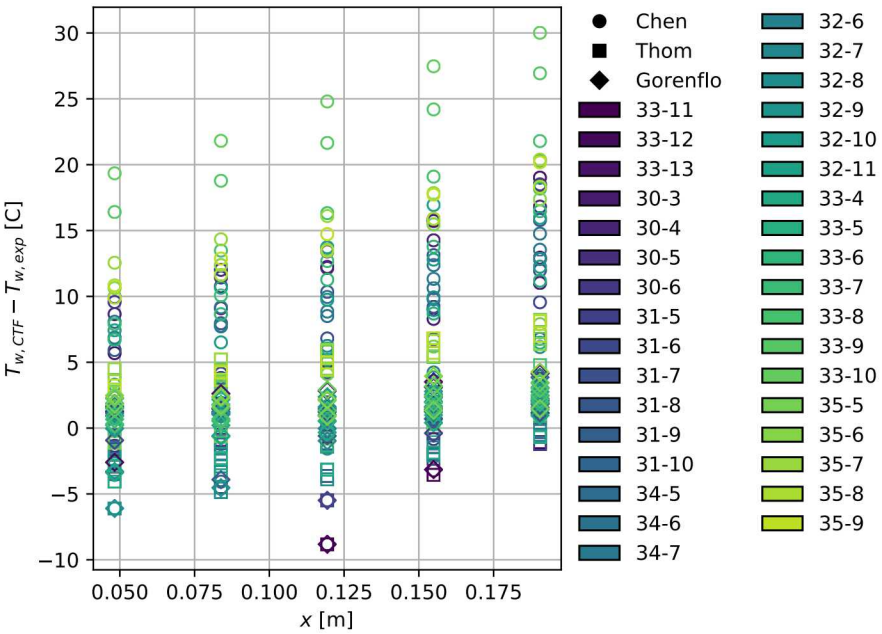

Figure 3.1: Rohsenow validation results as a function of spatial location

norm is taken over all three correlation options, since all three follow the same trend with respect to axial location. This supports the conclusion that all correlations are less accurate as the fluid temperature becomes closer to saturation.

Table 3.1: Rohsenow validation metrics as a function of correlation choice

Correlation	`IHTC`	mean [°C]	stdev [°C]	RMSE [°C]
Chen	1	9.5	7.1	11.9
Thom	2	0.9	3.0	3.1
Gorenflo	3	1.1	2.0	2.3

3.2 WALT

In 2005, a single rod thermal hydraulic facility was constructed at the Westinghouse Science and Technology Center in Pennsylvania. This loop has been named Westinghouse Advanced Loop Tester (WALT) and was designed to simulate PWR crud buildup [31]. Water flows through an 18.3 in long annulus with an approximate flow area of 0.6 m^2. A ZIRLO heated tube is equipped with four thermocouples located at different azimuthal angles at the same axial location. The thermocouples measure the inside tube temperature, and a simple heat conduction solution is used

Table 3.2: Rohsenow validation metrics as a function of thermocouple location

Thermocouple	location [m]	mean [°C]	stdev [°C]	RMSE [°C]
2	0.048	5.4	5.9	8.0
3	0.084	7.3	6.0	9.5
4	0.119	8.6	7.0	11.1
5	0.155	11.5	6.5	13.2
6	0.191	14.4	6.2	15.7

to approximate the outside tube temperature.

Though most of the WALT tests were used to create simulated crud and measure its thermal conductivity, a series of *clean rod* tests were initially performed. In this work, a separate effects validation study is conducted using these tests. In these tests, the heat flux was sequentially raised and temperature measurements were taken after the system was run for an extended period of time. Here, we assume that this time was sufficient to achieve steady state. This allows the construction of a so-called boiling curve, which can be compared to theory. This provided initial confidence in the experimental setup before including the more complex crud cases.

The WALT report [31] does not provide the tube outside temperatures that are calculated by CTF, so they must be approximated. Since the facility (and the code input) is completely symmetric, the thermocouple results are expected to be approximately the same. Therefore, the average of the four thermocouple measurements is used to calculate the surface temperature. This temperature is approximated as [31, Equation A-7]

$$T_{out} = T_{in} - \frac{q'''}{4k}\left[2r_{in}^2 \ln\left(\frac{r_{in}}{r_{out}} - r_{in}^2 + r_{out}^2\right)\right]. \tag{3.4}$$

The thermal conductivity of ZIRLO is approximated using a linear function of temperature [31, Equation 5-11] (note that this equation is in british units, temperature is in °F and thermal conductivity in btu/hr/ft/°F)

$$k = 8.1802 + 0.0026T \tag{3.5}$$

This facility is modeled in CTF using a single rod-centered channel with twenty axial nodes. The flow area, wetted perimeter, and rod diameter are set consistent with the geometry of the facility. The measured pressure is used as the outlet pressure boundary condition, the inlet boundary conditions are determined by the experimentally reported inlet temperature and mass flux. For each run, the wall temperature distribution is extracted from the code output. Linear interpolation

is used to approximate the wall temperature at the thermocouple location, which is then compared to the experimental value.

The difference between CTF and experimentally calculated wall temperatures are shown in Figure 3.2. The colors indicate which experiment is being represented (see Appendix B for the experimental conditions, measurements, and individual results for each individual experiment). The different correlations are tested: Chen, Thom, and Gorenflo. In general, the Chen correlation over estimates the wall superheat. The Gorenflo correlation is slightly more accurate than the Thom correlation. It also appears that all correlations are less accurate as the heat flux increases.

A few cases have very large over-predictions of wall temperature, even when using the Thom or Gorenflo correlations. These cases correspond to case 110a and 111b, which are the only two cases with lower inlet temperatures than other cases. This is demonstrated in Figure 3.3 by arranging the residuals with respect to inlet temperature.

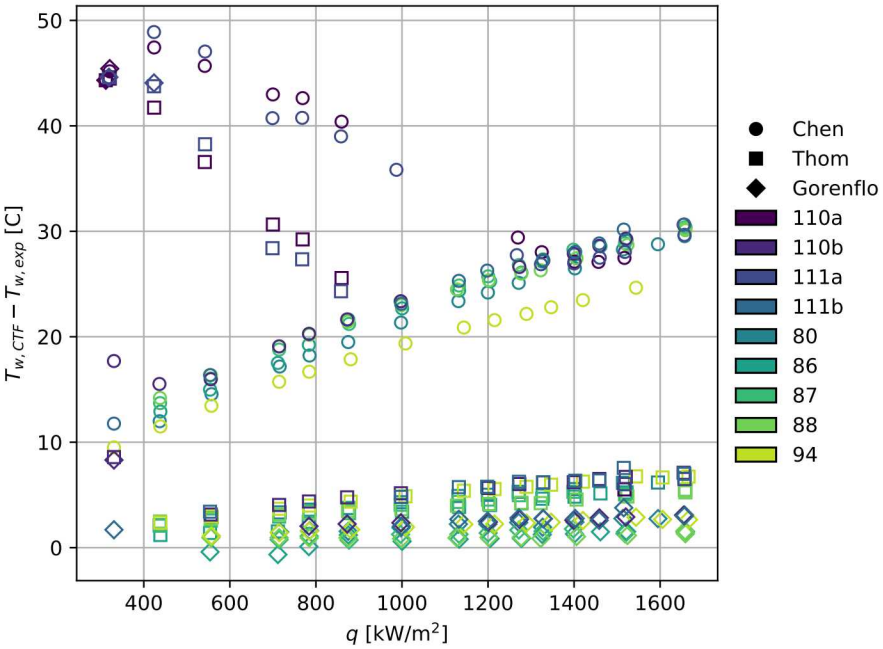

Figure 3.2: WALT validation results as a function of heat flux

The previously made observations are quantified using validation metrics. Table 3.3 shows the mean, standard deviation, and RMSE for each choice of correlation. Again, it is quantitatively demonstrated that the correlations can be ranked in order of accuracy: Gorenflo, Thom, then Chen. Table 3.4 shows the validation metrics for each individual experiment. All three correlation options are included in these norms, since they all follow the same trend with respect to experiment. Note that the 110a and 111a experiments have much larger mean and RMSE than all other cases. This demonstrates the large inaccuracy for the low temperature cases.

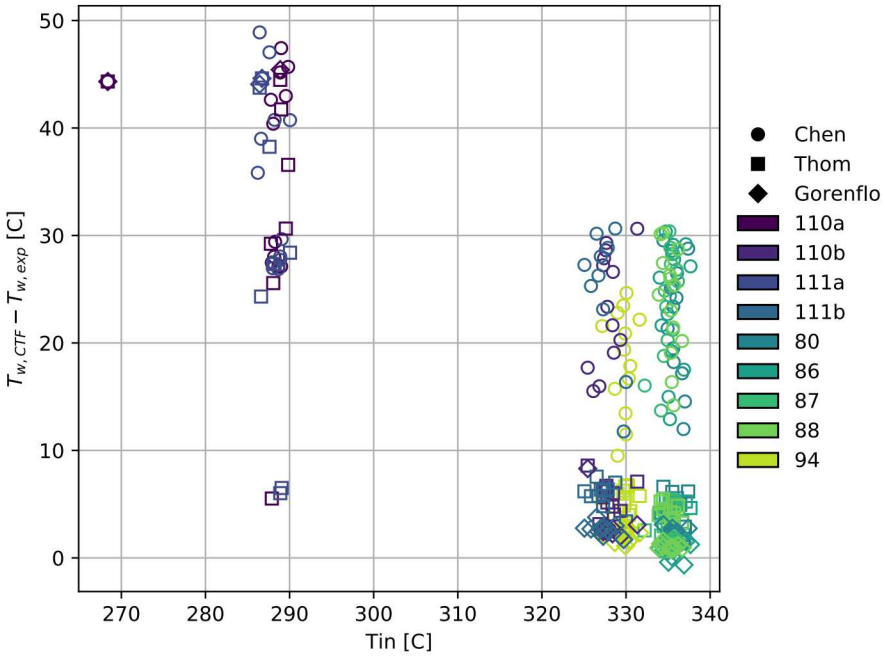

Figure 3.3: WALT validation results as a function of inlet temperature

Table 3.3: WALT validation metrics as a function of correlation choice

Correlation	`IHTC`	mean [°C]	stdev [°C]	RMSE [°C]
Chen	1	25.7	8.3	27.1
Thom	2	8.4	10.4	13.3
Gorenflo	3	3.8	9.0	9.7

Table 3.4: WALT validation metrics for each experiment

Experiment	mean [°C]	stdev [°C]	RMSE [°C]
80	9.7	9.6	84.6
86	9.7	10.7	95.8
87	10.1	10.4	88.1
88	9.8	10.5	92.1
94	8.5	7.5	71.7
110a	36.2	10.2	176.2
110b	11.2	9.6	89.6
111a	33.5	11.4	170.0
111b	11.1	10.3	83.2

4. Conclusion

In this work, subcooled boiling heat transfer was examined as a first step towards qualifying VERA crud modeling. Since crud formation is very sensitive to boiling, a correct understanding of the underlying physics in an important step towards understanding this complex multi-physics phenomenon. To achieve this, two separate studies were performed: a comparison of various subcooled boiling models to a variety of experimental data, and a separate effects validation of the subcooled boiling models available in CTF.

The comparison of subcooled boiling models to experimental data sets showed that all correlations generally underpredict the boiling heat flux. In the nuclear industry, the underprediction of surface heat flux will result in an overprediction of fuel temperatures, which is conservative. Differences between the predicted and measured heat fluxes are relatively large, ranging up to an order of magnitude. This is likely due to the large uncertainties in the boiling process, experimental uncertainties, and relatively small ranges of applicability for each model.

The CTF separate effects validation of the Rohsenow [23] and WALT [31] data was completed. For these two datasets, the correlations ranked from most to least accurate are: Gorenflo, Thom, and Chen. Chen was anticipated to be the least accurate, as it was originally formulated using low pressure experiments. Therefore, conventional wisdom dictates that the Chen correlation should be used for low pressure cases and Thom correlation for high pressure cases [32]. In general, CTF overpredicted wall temperatures in the subcooled region. Additionally, the CTF wall temperatures were less accurate as heat flux increased and fluid temperature increased. For both datasets, some CTF simulations failed to converge to steady state as determined by CTF steady state indicators. For the Rohsenow data, the Gorenflo correlation failed to converge for several of the cases. For the WALT data, all three correlations failed to converge for different cases. It is unclear if these convergence failures are due to numerical issues in the code, or represent some physical oscillation that is not represented in the steady state experimental data.

The results in both chapters agree in that an underestimation in heat flux will correspond to an overestimation of wall temperature. The validation results for the Rohsenow data were slightly different between Chapter 2 and Chapter 3. This difference may be due to subtle differences in correlation implementation between the Python script in Chapter 2 and CTF results in Chapter 3. Additionally, Chapter 2 calculated validation metrics with respect to heat flux, whereas Chapter 3

used wall temperature as the quantity of interest. These quantities are related, but not through a purely linear relationship. Therefore, it is possible that this difference causes the inconsistencies in RMSE results.

Future work will include the incorporation of additional correlations into the analyses, including adding them as simulation options in CTF. In addition, more datasets can be harvested from the literature and incorporated into the analyses in this report, e.g., Brown [33] and Bergles [34, 35]. Finally, future work will require the validation of additional modeling considerations of crud formation and heat transfer, including the prediction of void creation in CTF, actual accumulation of the crud, and the boiling processes in the porous crud in Materials Performance and Optimization (MPO) Advanced Model for Boron Analysis (MAMBA).

Bibliography

[1] T. Wellock. *CRUD: Another Acronym Bites the Dust*. 2015. URL: https://public-blog.nrc-gateway.gov/2015/03/31/crud-another-acronym-bites-the-dust/.

[2] J. Chen. *On the Interaction Between Fuel CRUD and Water Chemistry in Nuclear Power Plants*. Tech. rep. SKI-00:5. Studsvik, 2000.

[3] Nuclear Regulatory Commission. *Information Notice No. 97–85: Effects of Crud Buildup and Boron Deposition on Power Distribution and Shutdown Margin*. https://www.nrc.gov/reading-rm/doc-collections/gen-comm/info-notices/1997/in97085.html.

[4] Electric Power Research Institute. *PWR Axial Offset Anomaly (AOA) Guidelines, Revision 1*. Tech. rep. 1008102. EPRI, 2004.

[5] *Boron-Induced Offset Anomaly*. Tech. rep. 30020000831. Version 3.1. Palo Alto, CA: Electric Power Research Institute, 2013.

[6] M. A. Krammen et al. "Methods for Modeling Local Fuel Rod Crud and Assessing Failure Risk". In: *Proceedings of the International Conference on Nuclear Engineering (ICONE17)*. ICONE17–75715. 2009, pp. 551–559. DOI: 10.1115/ICONE17-75715.

[7] J. Deshon et al. "Pressurized Water Reactor Fuel Crud and Corrosion Modeling". In: *Advanced Fuel Performance: Modeling and Simulation* 63.64 (2011). DOI: 10.1007/s11837-011-0141-z.

[8] M. P. Short et al. "Multiphysics Modeling of Porous CRUD Deposits in Nuclear Reactors". In: *Journal of Nuclear Materials* 443.1–3 (2013), pp. 579–587. DOI: j.jnucmat.2013.08.014.

[9] W. M. Rohsenow and H. Choi. *Heat, Mass, and Momentum Transfer*. Englewood Cliffs, NJ: Prentice-Hall, Inc., 1961.

[10] V. Mousseau and N. Dinh. *CASL Verification and Validation Plan*. Tech. rep. CASL-U-2016-1116-000/SAND2016-6338R. CASL, 2016.

[11] C. Jones et al. *Initial Verification and Validation Assessment for VERA*. Tech. rep. CASL-U-2017-1310-000. CASL, 2017.

[12] J. G. Collier and J. R. Thome. *Convective Boiling and Condensation*. third. Oxford, UK: Oxford University Press, 1996.

[13] R. T. Lahey and F. J. Moody. *The Thermal-Hydraulics of a Boiling Water Nuclear Reactor*. USA: American Nuclear Society, 1977.

[14] J. C. Chen. "Correlation for Boiling Heat Transfer to Saturated Fluids in Convective Flow". In: *Industrial Engineering Chemistry Process Design and Development* 5.3 (1966). DOI: 10.1021/i260019a023.

[15] J. R. S. Thom et al. "Boiling in Sub-Cooled Water During Flow Up Heated Tubes or Annuli". In: *Proceedings of the Institution of Mechanical Engineers* 180.3 (1965). DOI: 10.1243/PIME_CONF_1965_180_117_02.

[16] D. Gorenflo and D. Kenning. "Pool Boiling". In: *VDI Heat Atlas*. Ed. by VDI e. V. Berlin, Germany: Springer, 2009. DOI: 10.1007/978-3-540-77877-6.

[17] K. E. Gungor and R. H. S. Winterton. *A General Correlation for Flow Boiling in Tubes and Annuli*. Tech. rep. 3. 1986, pp. 351–358. DOI: 10.1016/0017-9310(86)90205-X.

[18] F. W. Dittus and L. M. K. Boelter. "Heat Transfer in Automobile Radiators of the Tubular Type". In: *Publications in Engineering 2*. University of California, Berkeley, 1930, pp. 443–461. DOI: 10.1016/0735-1933(85)90003-X.

[19] N. E. Todreas and M. S. Kazimi. *Nuclear Systems I Thermal Hydraulic Fundamentals*. Levittown, PA: Taylor & Francis, 1993.

[20] H. K. Forster and N. Zuber. "Dynamics of Vapor Bubbles and Boiling Heat Transfer". In: *Advances in Chemical Engineering and Science* 1.4 (1955), p. 531. DOI: 10.1002/aic.690010425.

[21] W. H. Jens and P. A. Lottes. *Analysis of Heat Transfer, Burnout, Pressure Drop and Density Data for High-Pressure Water*. Tech. rep. ANL Report ANL-4627. Argonne National Laboratory, 1951.

[22] R. L. Sani. "Downflow Boiling and Nonboiling Heat Transfer in a Uniformly Heated Tube". MA thesis. University of California, Berkeley, 1960.

[23] W. M. Rohsenow and J. A. Clark. *Heat Transfer and Pressure Drop Data for High Heat Flux Densities to Water at High Subcritical Pressures*. Tech. rep. N5ori-07827/NR035-267/DIC6627. Office of Naval Research, 1951.

[24] A. E. Bergles. *Untitled Memo*. personal communication. 1961.

[25] J. R. Stone. *Subcooled- and Net-Boiling Heat Transfer to Low-Pressure Water in Electrically Heated Tubes*. Tech. rep. NASA Technical Note D-6402. NASA, 1971.

[26] R. Salko et al. *CTF Validation and Verification Manual*. Tech. rep. CASL-U-2019-1887. CASL, 2019.

[27] Z. Karoutas et al. *Subcooled Boiling Data from Rod Bundles*. Tech. rep. 1003383. Electric Power Research Institute, 2002.

[28] G. Cubizolles. *NESTOR Project: OMEGA Thermal Hydraulic Tests: SSG Bundle Test Data Report*. Tech. rep. CEA, 2007.

[29] W. L. Oberkampf and C. J. Roy. *Verification and Validation in Scientific Computing*. first. Cambridge, UK: Cambridge University Press, 2010.

[30] W. M. Rohsenow, J. P. Hartnett, and E. N. Ganić. *Heat Transfer Fundamentals*. 2nd ed. New York: McGraw-Hill, 1985.

[31] Electric Power Research Institute. *Simulated Fuel Crud Thermal Conductivity Measurements Under Pressurized Water Reactor Conditions*. Tech. rep. 1022896. EPRI, 2011.

[32] N. W. Porter and M. N. Avramova. "Validation of CTF Pressure Drop and Void Predictions for the NUPEC BWR Database". In: *Nuclear Engineering and Design* 337 (Oct. 2018), pp. 291–299. DOI: 10.1016/j.nucengdes.2018.07.018.

[33] W. T. Brown. "A Study of Flow Surface Boiling". PhD thesis. Massachusetts Institute of Technology, 1967.

[34] A. E. Bergles and W. M. Rohsenow. *Forced-Convection Surface-Boiling Heat Transfer and Burnout in Tubes of Small Diameter*. Tech. rep. 8767-21. Massachusetts Institute of Technology National Magnet Laboratory, 1962.

[35] A. E. Bergles and W. M. Rohsenow. "The Determination of Forced-Convection Surface-Boiling Heat Transfer". In: *Journal of Heat Transfer* 86.3 (1964), pp. 365–372. DOI: 10.1115/1.3688697.

A. Rohsenow Data and Results

Table A.1: Boundary condition and measured data for Rohsenow experiments. Units and precision are consistent with the original report [23]. Missing thermocouple measurements were excluded from the original report for an unknown reason.

Experiment	P psi	T_{in} °F	G Mlbm/hr/ft^2	q'' Mbtu/hr/ft^2	T_2 °F	T_3 °F	T_4 °F	T_5 °F	T_6 °F	T_{out} °F
33-11	2000	386	1618	2.53	–	–	643.5	643.5	642.5	470
33-12	2000	398	1610	2.76	642.0	643.5	644.0	643.0	641.5	491
33-13	2000	403	1602	3.00	644.5	644.5	644.5	643.5	642.5	503
30-3	2000	436	1051	1.78	642.5	643.5	644.5	644.5	643.5	523
30-4	2000	440	1052	2.03	643.0	643.5	645.0	645.0	644.0	539
30-5	2000	428	1059	2.23	644.5	645.0	646.5	646.0	645.0	537
30-6	2000	424	1059	2.20	643.0	644.0	644.0	644.0	643.0	523
31-5	2000	431	1063	1.54	–	–	643.0	643.0	643.0	504
31-6	2000	435	1060	1.74	642.5	643.5	644.5	644.5	643.5	519
31-7	2000	421	1057	1.92	643.5	644.5	644.5	644.5	643.5	514
31-8	2000	420	1057	2.10	644.5	645.5	645.5	644.5	643.5	520
31-9	2000	340	1130	2.34	–	645.0	647.0	646.0	645.0	454
31-10	2000	340	1118	2.54	643.5	645.5	646.5	644.5	643.5	464
34-5	2000	387	541	1.47	641.5	643.0	644.5	643.5	642.2	527
34-6	2000	376	545	1.62	642.5	643.5	645.0	643.5	642.0	531
34-7	2000	309	550	1.82	643.0	644.0	645.0	643.5	642.5	487
32-6	1500	439	1552	1.84	604.0	607.0	610.0	609.0	608.5	500
32-7	1500	431	1552	2.10	608.5	610.0	611.0	609.5	609.0	501
32-8	1500	390	1618	2.29	600.5	607.0	609.5	609.0	608.5	468
32-9	1500	397	1610	2.42	607.0	609.5	610.0	609.0	608.5	478
32-10	1500	397	1610	2.59	610.0	610.5	610.5	610.5	610.0	484
32-11	1500	396	1593	2.75	611.0	611.0	611.0	610.5	609.5	489
33-4	1500	430	1051	1.42	606.0	608.5	610.0	609.5	609.0	499
33-5	1500	425	1059	1.62	609.5	610.5	610.5	610.0	609.5	504
33-6	1500	426	1051	1.81	610.5	611.5	611.0	610.5	609.5	515
33-7	1500	422	1051	1.91	611.5	612.0	611.5	610.5	609.5	517
33-8	1500	426	1050	2.05	613.0	612.5	611.5	610.5	609.5	527
33-9	1500	427	1051	2.31	612.0	612.0	611.0	610.5	609.5	539
33-10	1500	413	1057	2.59	611.5	611.5	610.5	610.0	609.5	534
35-5	1500	376	543	1.14	605.0	606.0	608.0	607.5	607.5	487
35-6	1500	396	541	1.39	604.0	604.0	605.0	604.5	604.0	528
35-7	1500	385	541	1.56	604.5	604.5	604.5	604.5	603.0	534
35-8	1500	309	559	1.81	606.5	606.5	606.5	605.5	604.5	485
35-9	1500	319	556	1.84	607.0	606.5	606.5	604.5	603.5	499

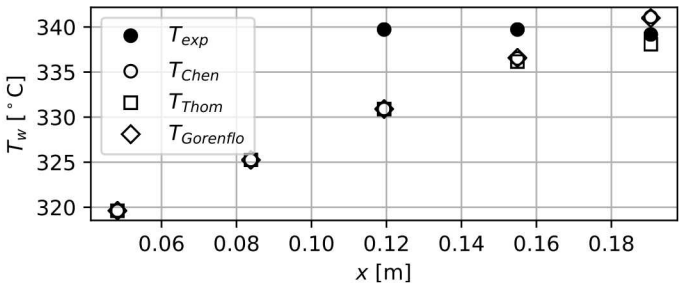

z m		T_{exp} °C	T_{chen} °C	T_{thom} °C	T_{gor} °C
0.048	T_w	–	319.6	319.6	319.6
0.084	T_w	–	325.2	325.2	325.2
0.119	T_w	339.7	330.9	330.9	330.9
0.155	T_w	339.7	336.5	336.2	336.6
0.191	T_w	339.2	341.1	338.1	341.0
0.239	T_f	243.3	243.1	243.1	243.1

Figure A.1: CTF and experimental results for Rohsenow experiment 33-11

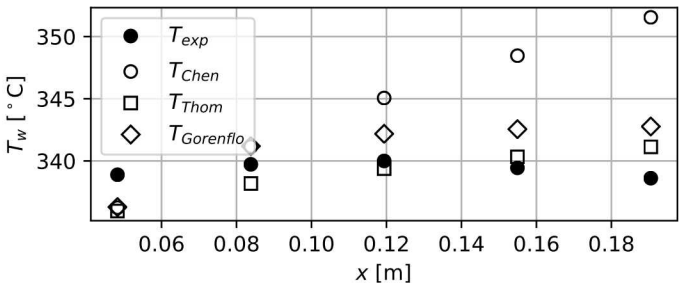

z m		T_{exp} °C	T_{chen} °C	T_{thom} °C	T_{gor} °C
0.048	T_w	338.9	336.2	336.0	336.3
0.084	T_w	339.7	341.2	338.2	341.2
0.119	T_w	340.0	345.1	339.4	342.2
0.155	T_w	339.4	348.5	340.3	342.6
0.191	T_w	338.6	351.5	341.1	342.8
0.239	T_f	255.0	253.6	253.6	253.6

Figure A.2: CTF and experimental results for Rohsenow experiment 33-12

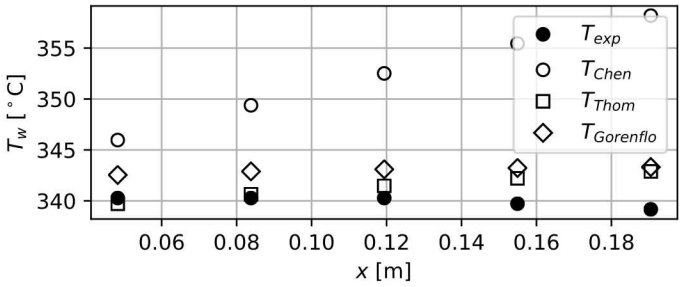

z m		T_{exp} °C	T_{chen} °C	T_{thom} °C	T_{gor} °C
0.048	T_w	340.3	346.0	339.7	342.5
0.084	T_w	340.3	349.4	340.7	342.9
0.119	T_w	340.3	352.5	341.5	343.1
0.155	T_w	339.7	355.4	342.2	343.2
0.191	T_w	339.2	358.2	342.9	343.3
0.239	T_f	261.7	260.5	260.6	260.6

Figure A.3: CTF and experimental results for Rohsenow experiment 33-13

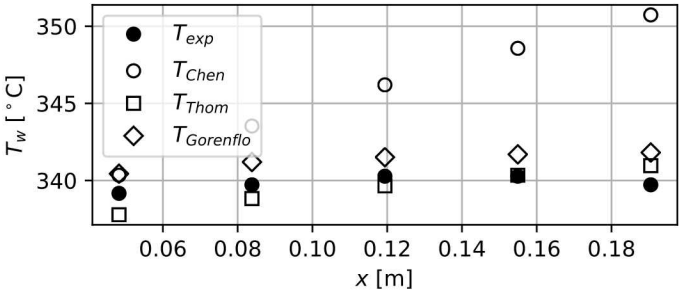

z m		T_{exp} °C	T_{chen} °C	T_{thom} °C	T_{gor} °C
0.048	T_w	339.2	340.3	337.8	340.4
0.084	T_w	339.7	343.5	338.8	341.2
0.119	T_w	340.3	346.2	339.6	341.5
0.155	T_w	340.3	348.6	340.3	341.7
0.191	T_w	339.7	350.7	341.0	341.8
0.239	T_f	272.8	272.4	272.5	272.5

Figure A.4: CTF and experimental results for Rohsenow experiment 30-3

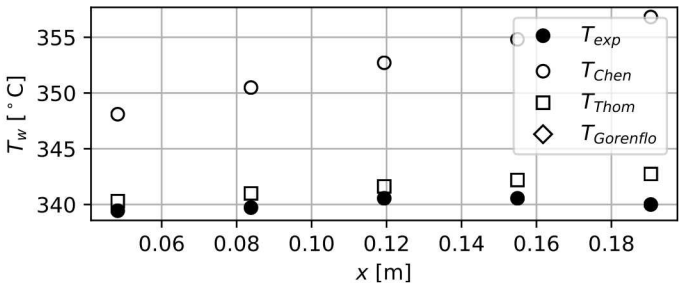

z m		T_{exp} °C	T_{chen} °C	T_{thom} °C	T_{gor} °C
0.048	T_w	339.4	348.1	340.3	–
0.084	T_w	339.7	350.5	341.0	–
0.119	T_w	340.6	352.7	341.6	–
0.155	T_w	340.6	354.8	342.2	–
0.191	T_w	340.0	356.8	342.7	–
0.239	T_f	281.7	280.6	280.7	–

Figure A.5: CTF and experimental results for Rohsenow experiment 30-4

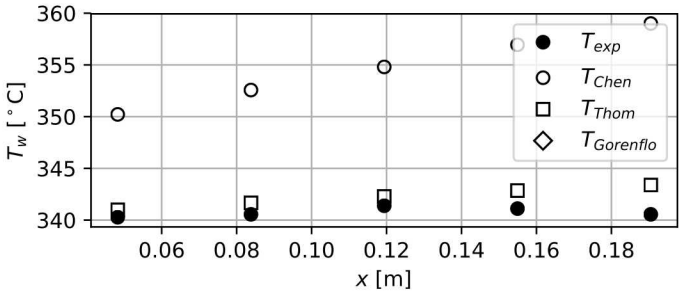

z m		T_{exp} °C	T_{chen} °C	T_{thom} °C	T_{gor} °C
0.048	T_w	340.3	350.2	341.0	–
0.084	T_w	340.6	352.6	341.7	–
0.119	T_w	341.4	354.8	342.3	–
0.155	T_w	341.1	356.9	342.9	–
0.191	T_w	340.6	359.0	343.4	–
0.239	T_f	280.6	279.2	279.4	–

Figure A.6: CTF and experimental results for Rohsenow experiment 30-5

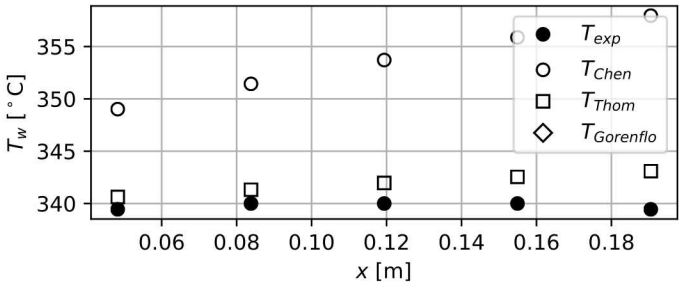

z m		T_{exp} °C	T_{chen} °C	T_{thom} °C	T_{gor} °C
0.048	T_w	339.4	349.0	340.6	–
0.084	T_w	340.0	351.4	341.3	–
0.119	T_w	340.0	353.7	342.0	–
0.155	T_w	340.0	355.9	342.6	–
0.191	T_w	339.4	358.0	343.1	–
0.239	T_f	272.8	276.5	276.7	–

Figure A.7: CTF and experimental results for Rohsenow experiment 30-6

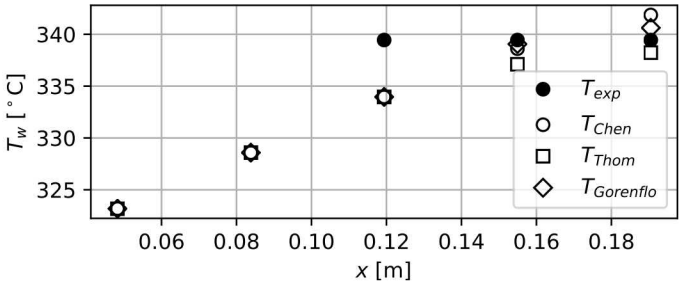

z m		T_{exp} °C	T_{chen} °C	T_{thom} °C	T_{gor} °C
0.048	T_w	–	323.2	323.2	323.2
0.084	T_w	–	328.6	328.6	328.6
0.119	T_w	339.4	334.0	334.0	334.0
0.155	T_w	339.4	338.6	337.1	339.1
0.191	T_w	339.4	341.9	338.2	340.6
0.239	T_f	262.2	263.2	263.2	263.2

Figure A.8: CTF and experimental results for Rohsenow experiment 31-5

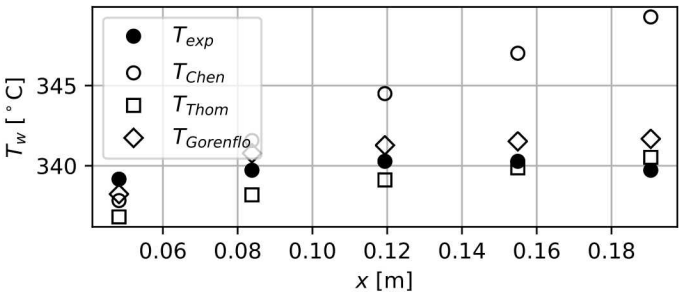

z m		T_{exp} °C	T_{chen} °C	T_{thom} °C	T_{gor} °C
0.048	T_w	339.2	337.8	336.8	338.2
0.084	T_w	339.7	341.6	338.2	340.8
0.119	T_w	340.3	344.5	339.1	341.3
0.155	T_w	340.3	347.0	339.9	341.5
0.191	T_w	339.7	349.3	340.5	341.7
0.239	T_f	270.6	270.5	270.5	270.5

Figure A.9: CTF and experimental results for Rohsenow experiment 31-6

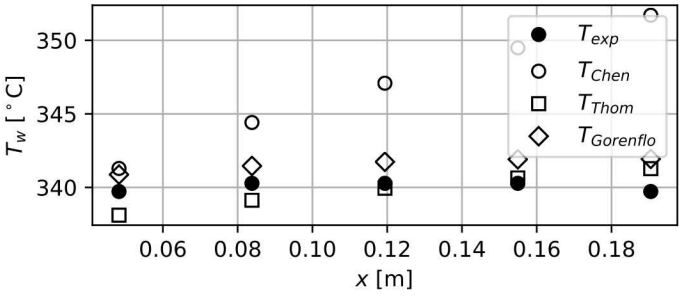

z m		T_{exp} °C	T_{chen} °C	T_{thom} °C	T_{gor} °C
0.048	T_w	339.7	341.3	338.1	340.9
0.084	T_w	340.3	344.4	339.1	341.5
0.119	T_w	340.3	347.1	339.9	341.7
0.155	T_w	340.3	349.5	340.6	341.9
0.191	T_w	339.7	351.7	341.3	341.9
0.239	T_f	267.8	268.1	268.2	268.2

Figure A.10: CTF and experimental results for Rohsenow experiment 31-7

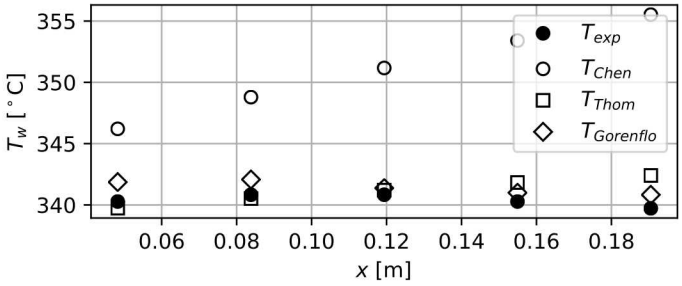

z m		T_{exp} °C	T_{chen} °C	T_{thom} °C	T_{gor} °C
0.048	T_w	340.3	346.2	339.7	341.9
0.084	T_w	340.8	348.8	340.5	342.1
0.119	T_w	340.8	351.2	341.2	341.4
0.155	T_w	340.3	353.4	341.8	341.0
0.191	T_w	339.7	355.5	342.4	340.8
0.239	T_f	271.1	272.2	272.3	272.3

Figure A.11: CTF and experimental results for Rohsenow experiment 31-8

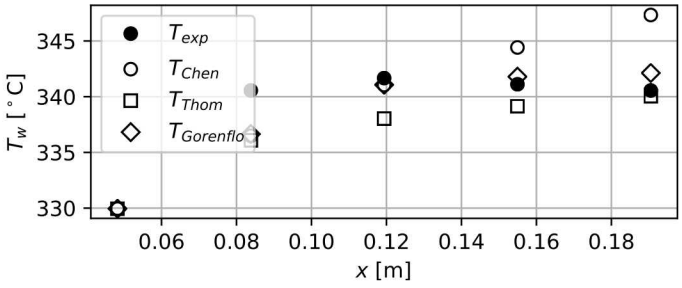

z m		T_{exp} °C	T_{chen} °C	T_{thom} °C	T_{gor} °C
0.048	T_w	–	330.0	330.0	330.0
0.084	T_w	340.6	336.5	336.1	336.6
0.119	T_w	341.7	341.0	338.0	341.1
0.155	T_w	341.1	344.4	339.1	341.8
0.191	T_w	340.6	347.3	340.0	342.1
0.239	T_f	234.4	233.7	233.7	233.8

Figure A.12: CTF and experimental results for Rohsenow experiment 31-9

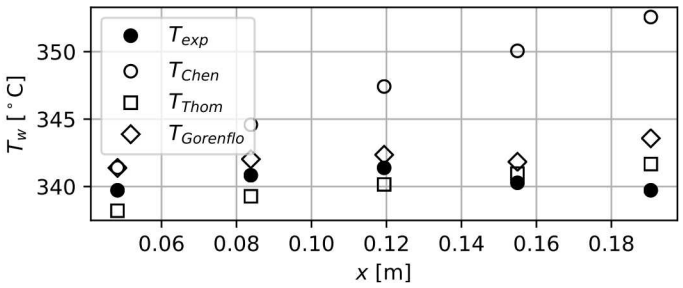

z m		T_{exp} °C	T_{chen} °C	T_{thom} °C	T_{gor} °C
0.048	T_w	339.7	341.4	338.2	341.4
0.084	T_w	340.8	344.6	339.3	342.0
0.119	T_w	341.4	347.4	340.2	342.4
0.155	T_w	340.3	350.1	341.0	341.8
0.191	T_w	339.7	352.6	341.7	343.6
0.239	T_f	240.0	239.5	239.6	239.6

Figure A.13: CTF and experimental results for Rohsenow experiment 31-10

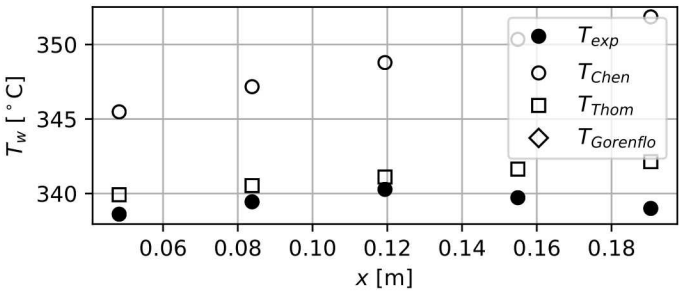

z m		T_{exp} °C	T_{chen} °C	T_{thom} °C	T_{gor} °C
0.048	T_w	338.6	345.5	339.9	–
0.084	T_w	339.4	347.2	340.5	–
0.119	T_w	340.3	348.8	341.1	–
0.155	T_w	339.7	350.3	341.6	–
0.191	T_w	339.0	351.9	342.1	–
0.239	T_f	275.0	275.3	275.6	–

Figure A.14: CTF and experimental results for Rohsenow experiment 34-5

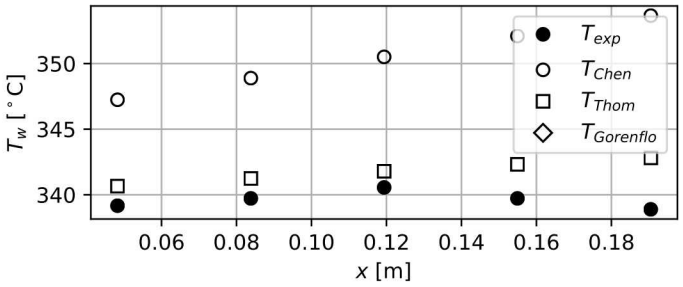

z m		T_{exp} °C	T_{chen} °C	T_{thom} °C	T_{gor} °C
0.048	T_w	339.2	347.2	340.7	–
0.084	T_w	339.7	348.9	341.2	–
0.119	T_w	340.6	350.5	341.8	–
0.155	T_w	339.7	352.1	342.3	–
0.191	T_w	338.9	353.7	342.8	–
0.239	T_f	277.2	276.6	277.0	–

Figure A.15: CTF and experimental results for Rohsenow experiment 34-6

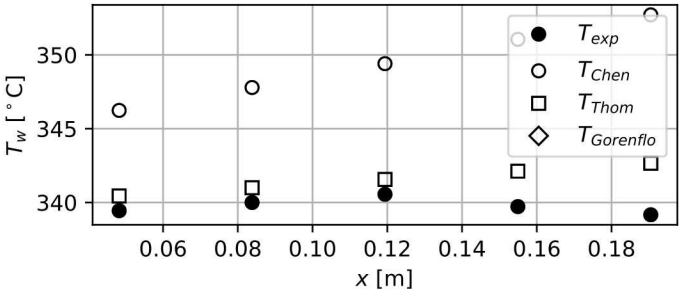

z m		T_{exp} °C	T_{chen} °C	T_{thom} °C	T_{gor} °C
0.048	T_w	339.4	346.2	340.4	–
0.084	T_w	340.0	347.8	341.0	–
0.119	T_w	340.6	349.4	341.6	–
0.155	T_w	339.7	351.1	342.1	–
0.191	T_w	339.2	352.7	342.7	–
0.239	T_f	252.8	253.0	253.4	–

Figure A.16: CTF and experimental results for Rohsenow experiment 34-7

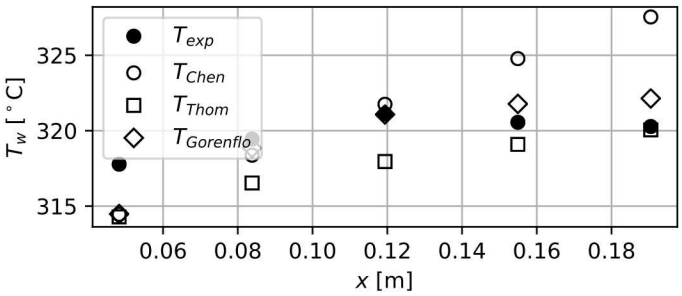

z m		T_{exp} °C	T_{chen} °C	T_{thom} °C	T_{gor} °C
0.048	T_w	317.8	314.5	314.3	314.5
0.084	T_w	319.4	318.4	316.5	318.9
0.119	T_w	321.1	321.8	318.0	321.1
0.155	T_w	320.6	324.8	319.1	321.8
0.191	T_w	320.3	327.5	320.1	322.1
0.239	T_f	260.0	259.8	259.9	259.9

Figure A.17: CTF and experimental results for Rohsenow experiment 32-6

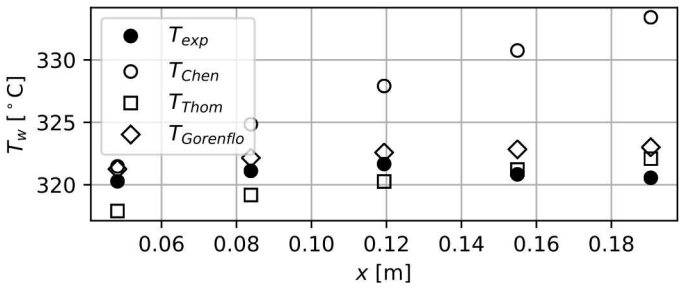

z m		T_{exp} °C	T_{chen} °C	T_{thom} °C	T_{gor} °C
0.048	T_w	320.3	321.5	317.9	321.3
0.084	T_w	321.1	324.8	319.2	322.2
0.119	T_w	321.7	327.9	320.3	322.6
0.155	T_w	320.8	330.8	321.2	322.8
0.191	T_w	320.6	333.4	322.1	323.0
0.239	T_f	260.6	260.3	260.3	260.3

Figure A.18: CTF and experimental results for Rohsenow experiment 32-7

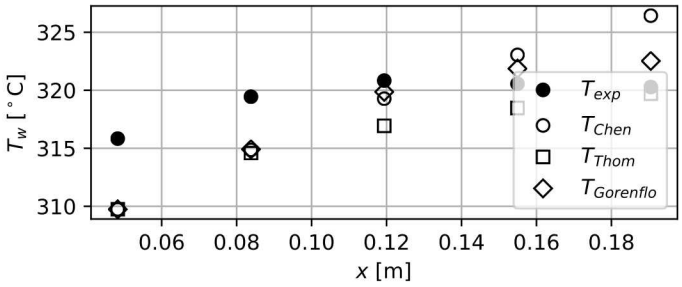

z m		T_{exp} °C	T_{chen} °C	T_{thom} °C	T_{gor} °C
0.048	T_w	315.8	309.7	309.7	309.7
0.084	T_w	319.4	314.9	314.6	314.9
0.119	T_w	320.8	319.3	316.9	319.9
0.155	T_w	320.6	323.0	318.5	321.9
0.191	T_w	320.3	326.4	319.7	322.5
0.239	T_f	242.2	240.7	240.7	240.7

Figure A.19: CTF and experimental results for Rohsenow experiment 32-8

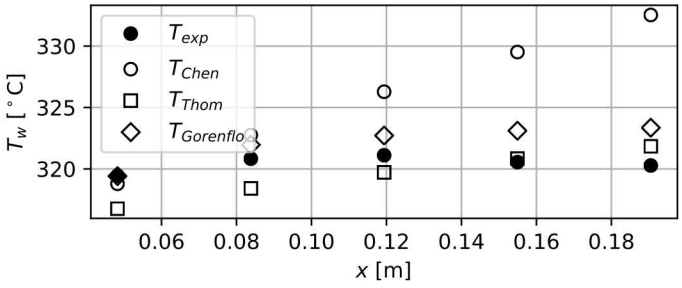

z m		T_{exp} °C	T_{chen} °C	T_{thom} °C	T_{gor} °C
0.048	T_w	319.4	318.8	316.8	319.4
0.084	T_w	320.8	322.8	318.4	322.0
0.119	T_w	321.1	326.3	319.7	322.7
0.155	T_w	320.6	329.5	320.8	323.1
0.191	T_w	320.3	332.5	321.8	323.4
0.239	T_f	247.8	246.8	246.8	246.8

Figure A.20: CTF and experimental results for Rohsenow experiment 32-9

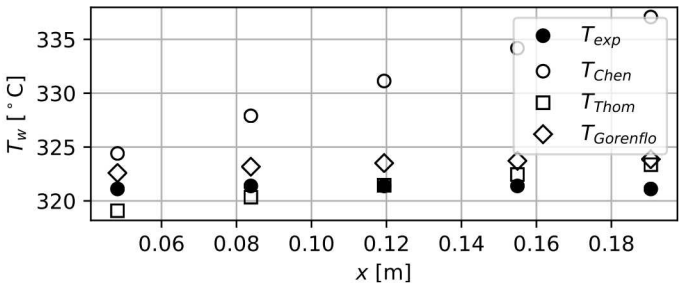

z m		T_{exp} °C	T_{chen} °C	T_{thom} °C	T_{gor} °C
0.048	T_w	321.1	324.4	319.1	322.6
0.084	T_w	321.4	327.9	320.3	323.2
0.119	T_w	321.4	331.1	321.5	323.5
0.155	T_w	321.4	334.2	322.4	323.7
0.191	T_w	321.1	337.1	323.4	323.9
0.239	T_f	251.1	249.8	249.8	249.8

Figure A.21: CTF and experimental results for Rohsenow experiment 32-10

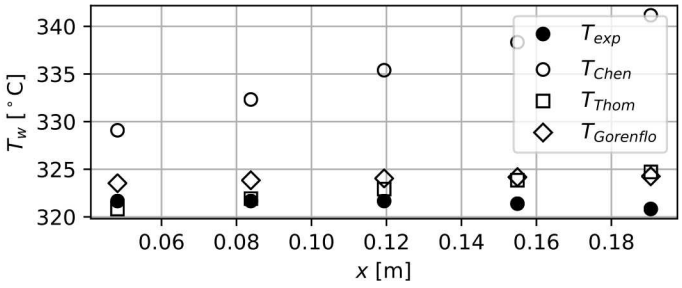

z m		T_{exp} °C	T_{chen} °C	T_{thom} °C	T_{gor} °C
0.048	T_w	321.7	329.1	320.8	323.5
0.084	T_w	321.7	332.3	321.9	323.8
0.119	T_w	321.7	335.4	322.9	324.0
0.155	T_w	321.4	338.3	323.9	324.2
0.191	T_w	320.8	341.2	324.7	324.3
0.239	T_f	253.9	252.5	252.6	252.6

Figure A.22: CTF and experimental results for Rohsenow experiment 32-11

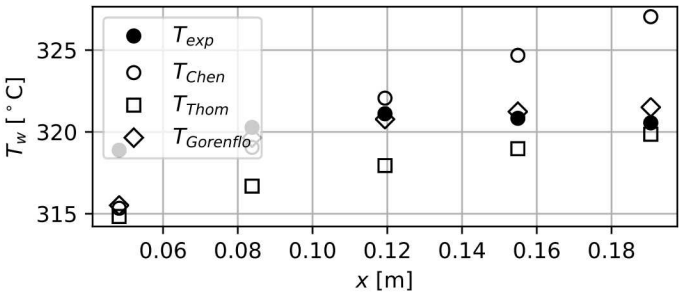

z m		T_{exp} °C	T_{chen} °C	T_{thom} °C	T_{gor} °C
0.048	T_w	318.9	315.3	314.8	315.5
0.084	T_w	320.3	319.1	316.7	319.6
0.119	T_w	321.1	322.1	317.9	320.8
0.155	T_w	320.8	324.7	319.0	321.2
0.191	T_w	320.6	327.0	319.9	321.5
0.239	T_f	259.4	259.7	259.7	259.7

Figure A.23: CTF and experimental results for Rohsenow experiment 33-4

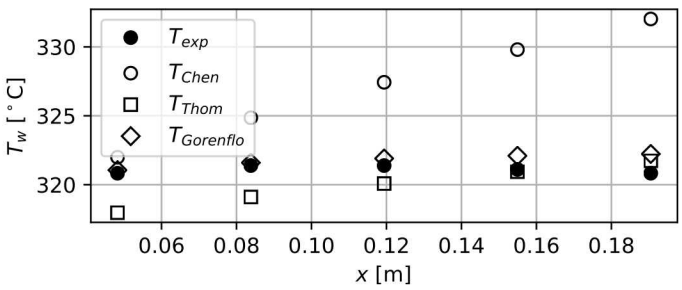

z m		T_{exp} °C	T_{chen} °C	T_{thom} °C	T_{gor} °C
0.048	T_w	320.8	322.0	318.0	321.1
0.084	T_w	321.4	324.9	319.1	321.6
0.119	T_w	321.4	327.4	320.1	321.9
0.155	T_w	321.1	329.8	320.9	322.1
0.191	T_w	320.8	332.0	321.7	322.2
0.239	T_f	262.2	262.0	262.0	262.1

Figure A.24: CTF and experimental results for Rohsenow experiment 33-5

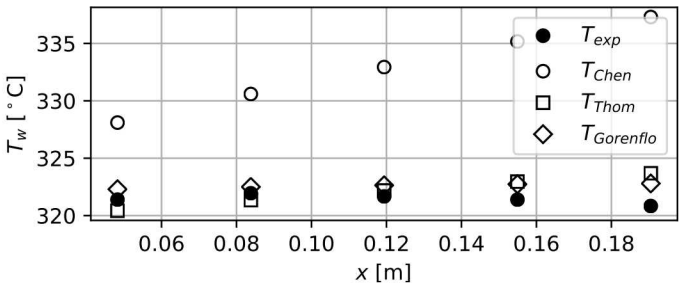

z m		T_{exp} °C	T_{chen} °C	T_{thom} °C	T_{gor} °C
0.048	T_w	321.4	328.1	320.4	322.3
0.084	T_w	321.9	330.6	321.3	322.5
0.119	T_w	321.7	332.9	322.2	322.6
0.155	T_w	321.4	335.2	323.0	322.7
0.191	T_w	320.8	337.3	323.7	322.8
0.239	T_f	268.3	267.6	267.8	267.8

Figure A.25: CTF and experimental results for Rohsenow experiment 33-6

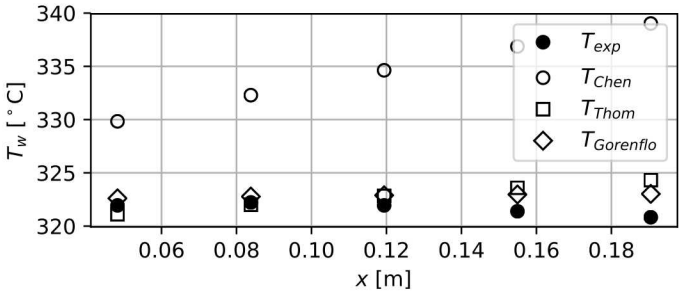

z m		T_{exp} °C	T_{chen} °C	T_{thom} °C	T_{gor} °C
0.048	T_w	321.9	329.8	321.1	322.6
0.084	T_w	322.2	332.3	322.0	322.8
0.119	T_w	321.9	334.6	322.8	322.9
0.155	T_w	321.4	336.9	323.6	323.0
0.191	T_w	320.8	339.0	324.3	323.0
0.239	T_f	269.4	268.2	268.3	268.3

Figure A.26: CTF and experimental results for Rohsenow experiment 33-7

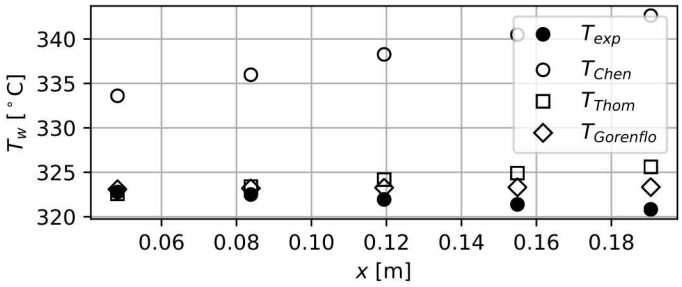

z m		T_{exp} °C	T_{chen} °C	T_{thom} °C	T_{gor} °C
0.048	T_w	322.8	333.6	322.6	323.1
0.084	T_w	322.5	336.0	323.4	323.2
0.119	T_w	321.9	338.3	324.2	323.3
0.155	T_w	321.4	340.5	324.9	323.3
0.191	T_w	320.8	342.6	325.6	323.3
0.239	T_f	275.0	273.7	273.9	274.0

Figure A.27: CTF and experimental results for Rohsenow experiment 33-8

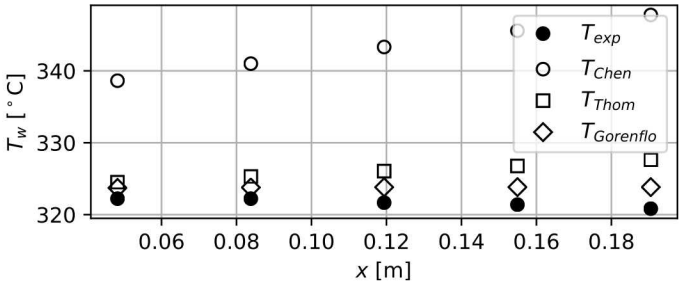

z m		T_{exp} °C	T_{chen} °C	T_{thom} °C	T_{gor} °C
0.048	T_w	322.2	338.6	324.5	323.7
0.084	T_w	322.2	341.0	325.3	323.8
0.119	T_w	321.7	343.3	326.1	323.8
0.155	T_w	321.4	345.6	326.8	323.8
0.191	T_w	320.8	347.8	327.6	323.8
0.239	T_f	281.7	279.4	280.3	280.9

Figure A.28: CTF and experimental results for Rohsenow experiment 33-9

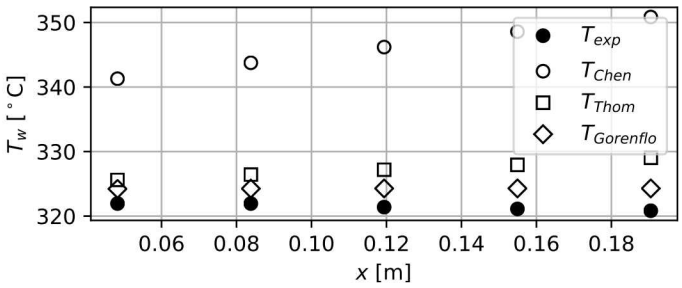

z m		T_{exp} °C	T_{chen} °C	T_{thom} °C	T_{gor} °C
0.048	T_w	321.9	341.3	325.6	324.2
0.084	T_w	321.9	343.8	326.4	324.3
0.119	T_w	321.4	346.2	327.2	324.3
0.155	T_w	321.1	348.6	327.9	324.3
0.191	T_w	320.8	350.8	329.0	324.3
0.239	T_f	278.9	278.3	279.7	280.6

Figure A.29: CTF and experimental results for Rohsenow experiment 33-10

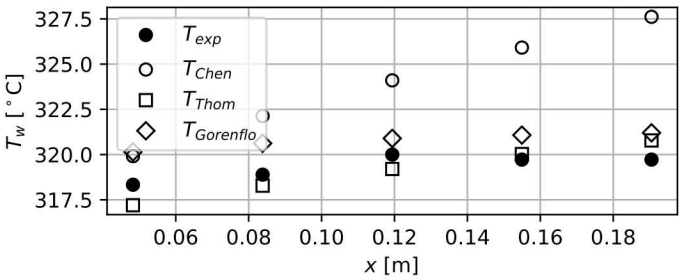

z m		T_{exp} °C	T_{chen} °C	T_{thom} °C	T_{gor} °C
0.048	T_w	318.3	319.9	317.2	320.1
0.084	T_w	318.9	322.1	318.3	320.6
0.119	T_w	320.0	324.1	319.2	320.9
0.155	T_w	319.7	325.9	320.0	321.1
0.191	T_w	319.7	327.6	320.8	321.2
0.239	T_f	252.8	252.6	252.8	252.8

Figure A.30: CTF and experimental results for Rohsenow experiment 35-5

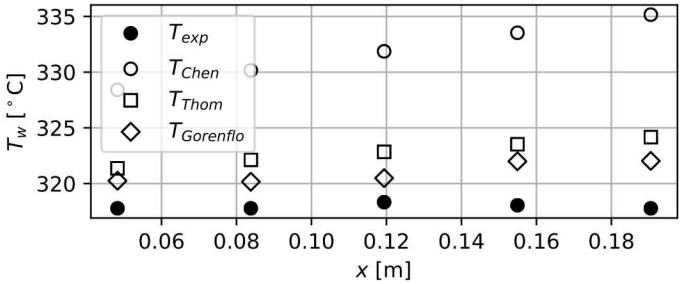

z m		T_{exp} °C	T_{chen} °C	T_{thom} °C	T_{gor} °C
0.048	T_w	317.8	328.4	321.4	320.3
0.084	T_w	317.8	330.2	322.1	320.2
0.119	T_w	318.3	331.9	322.8	320.5
0.155	T_w	318.1	333.5	323.5	322.0
0.191	T_w	317.8	335.2	324.2	322.0
0.239	T_f	275.6	274.9	275.4	275.6

Figure A.31: CTF and experimental results for Rohsenow experiment 35-6

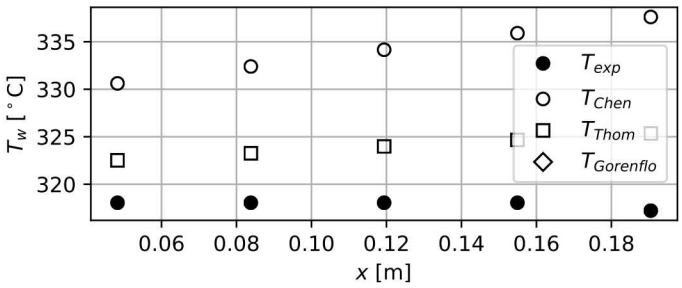

z m		T_{exp} °C	T_{chen} °C	T_{thom} °C	T_{gor} °C
0.048	T_w	318.1	330.6	322.5	–
0.084	T_w	318.1	332.4	323.3	–
0.119	T_w	318.1	334.2	324.0	–
0.155	T_w	318.1	335.9	324.7	–
0.191	T_w	317.2	337.6	325.3	–
0.239	T_f	278.9	276.9	277.9	–

Figure A.32: CTF and experimental results for Rohsenow experiment 35-7

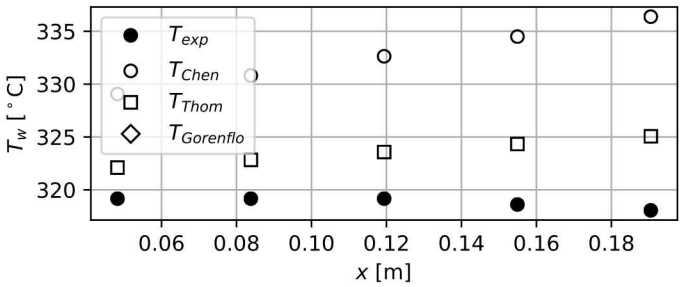

z m		T_{exp} °C	T_{chen} °C	T_{thom} °C	T_{gor} °C
0.048	T_w	319.2	329.1	322.1	–
0.084	T_w	319.2	330.8	322.8	–
0.119	T_w	319.2	332.6	323.6	–
0.155	T_w	318.6	334.5	324.3	–
0.191	T_w	318.1	336.4	325.1	–
0.239	T_f	251.7	250.5	251.0	–

Figure A.33: CTF and experimental results for Rohsenow experiment 35-8

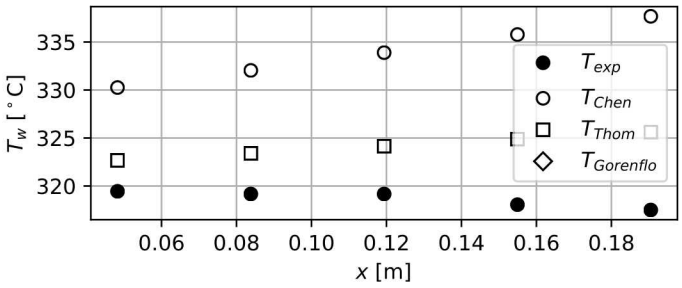

z m		T_{exp} °C	T_{chen} °C	T_{thom} °C	T_{gor} °C
0.048	T_w	319.4	330.3	322.7	–
0.084	T_w	319.2	332.0	323.4	–
0.119	T_w	319.2	333.9	324.1	–
0.155	T_w	318.1	335.8	324.9	–
0.191	T_w	317.5	337.7	325.6	–
0.239	T_f	259.4	257.4	257.9	–

Figure A.34: CTF and experimental results for Rohsenow experiment 35-9

B. WALT Data and Results

Table B.1: Geometric information for WALT experiments. Units and precision are consistent with the original report [31].

Experiment	D_o in	D_i in	A_f in^2	P_w in	L in
80	0.374	0.329	0.36187	3.60969	18.322
86	0.374	0.329	0.57236	4.10292	18.322
87	0.374	0.329	0.57236	4.10292	18.322
88	0.374	0.329	0.57236	4.10292	18.322
94	0.374	0.329	0.57236	4.10292	18.322
110a	0.374	0.329	0.57236	4.10292	18.322
110b	0.374	0.329	0.57236	4.10292	18.322
111a	0.374	0.329	0.57236	4.10292	18.322
111b	0.374	0.329	0.57236	4.10292	18.322

Table B.2: Boundary condition and measured data for WALT experiments. Units and precision are consistent with the original report [31]. Thermocouple measurements that are inconsistent with surrounding measurements are colored red and excluded from the validation study.

Experiment	P psi	T_{in} °F	G Mlbm/hr/ft^2	q'' Mbtu/hr/ft^2	T_1 °F	T_2 °F	T_3 °F	T_4 °F
80	2244.7	638.3	1.8944	0.1385	669.9	670.3	670.2	670.5
	2266.2	638.6	1.8917	0.1767	674.7	675.1	675.1	675.4
	2264.5	638.0	1.8957	0.2269	680.1	680.5	680.6	680.9
	2266.5	636.2	1.9043	0.2489	682.4	682.8	682.9	683.1
	2258.8	636.1	1.9029	0.2774	685.2	685.6	685.6	686.0
	2265.1	634.9	1.9171	0.3163	689.0	689.5	689.7	689.9
	2264.8	636.1	1.9066	0.3586	693.0	693.3	693.5	693.9
	2265.2	636.8	1.9022	0.3803	695.3	695.6	695.9	696.2
	2264.5	635.6	1.9078	0.4030	697.3	697.5	698.1	698.3
	2264.8	637.6	1.8963	0.4206	700.0	699.9	700.5	701.4
	2264.7	636.9	1.9031	0.4444	701.5	701.9	702.2	702.6
	2234.8	635.9	1.8964	0.4798	702.7	703.3	703.6	704.1
	2264.7	639.3	1.8856	0.5056	707.1	707.6	708.0	708.4
	2265.2	634.0	1.9222	0.5252	708.5	709.2	709.4	709.7
86	2263.6	635.4	1.3013	0.1390	674.1	674.6	673.6	659.2
	2265.1	635.1	1.3042	0.1756	678.5	679.2	678.5	662.7
	2265.6	638.4	1.2914	0.2256	684.8	685.5	684.5	668.1
	2268.3	635.8	1.2954	0.2484	686.1	686.8	685.8	668.0
	2265.4	633.6	1.3051	0.2775	687.7	688.5	687.9	684.9
	2270.1	634.9	1.2999	0.3171	693.6	694.2	693.2	690.5
	2270.5	635.4	1.2988	0.3591	697.8	698.5	697.3	694.4
	2270.6	636.0	1.2960	0.3819	700.1	700.7	699.7	696.7
	2264.6	633.2	1.3048	0.4050	702.3	702.8	701.7	698.7
	2264.1	639.8	1.2836	0.4204	703.0	703.6	702.6	699.8
	2267.4	636.3	1.2902	0.4441	705.7	706.1	705.1	702.4
	2265.6	635.8	1.2902	0.4632	706.1	707.0	706.1	706.2
	2268.8	636.1	1.2932	0.4817	709.4	709.8	708.7	705.9
	2267.7	638.8	1.2803	0.4825	709.3	709.6	708.7	706.0

Table B.2 continued

Experiment	P psi	T_{in} °F	G Mlbm/hr/ft^2	q'' Mbtu/hr/ft^2	T_1 °F	T_2 °F	T_3 °F	T_4 °F
	2272.7	634.5	1.2968	0.5259	714.1	714.4	713.4	710.6
87	2264.9	633.5	1.3100	0.1388	672.3	673.3	673.1	671.0
	2264.6	630.0	1.3187	0.1762	676.3	677.3	677.0	675.0
	2268.1	634.1	1.3021	0.2265	682.4	683.5	683.2	681.2
	2263.6	634.9	1.3028	0.2486	684.0	685.0	684.8	683.0
	2265.8	636.0	1.2916	0.2780	688.0	689.1	688.8	687.0
	2264.8	634.6	1.3000	0.3160	691.0	692.1	691.9	690.1
	2265.1	634.3	1.2996	0.3590	695.6	696.7	696.5	694.6
	2272.2	637.1	1.2899	0.3805	698.0	699.2	698.9	697.1
	2268.1	636.8	1.2877	0.4031	699.6	700.8	700.6	698.8
	2265.1	635.6	1.2967	0.4209	701.5	702.7	702.5	700.7
	2268.2	636.1	1.2954	0.4433	703.6	704.8	704.6	702.8
	2270.9	635.5	1.2909	0.4813	708.2	709.9	709.9	707.3
	2264.9	635.3	1.2923	0.5256	712.2	714.4	713.2	711.3
88	2264.9	636.2	1.3020	0.1387	671.7	671.6	672.3	671.9
	2270.0	635.8	1.3059	0.1762	676.5	676.4	677.1	676.7
	2265.0	635.6	1.3036	0.2265	681.9	681.8	682.5	682.2
	2265.8	638.0	1.2905	0.2487	684.5	684.4	685.0	684.8
	2265.4	636.1	1.3005	0.2772	687.5	687.5	688.1	687.8
	2265.7	635.6	1.2998	0.3166	691.8	691.9	692.6	692.2
	2265.5	633.0	1.3125	0.3575	696.0	696.1	696.8	696.4
	2274.2	636.3	1.3004	0.3811	699.0	699.1	699.6	699.2
	2289.1	635.5	1.3052	0.4049	702.2	702.3	703.0	702.6
	2290.2	635.4	1.3021	0.4192	704.0	704.1	704.7	704.3
	2282.5	633.9	1.3100	0.4456	706.0	706.1	706.7	706.3
	2282.9	637.1	1.2965	0.4831	709.7	709.8	710.4	710.0
	2290.9	633.9	1.3100	0.5254	713.8	713.8	714.4	714.0
	2281.5	633.4	1.3104	0.5258	713.8	713.8	714.4	714.0
94	2264.7	624.2	0.7833	0.1048	668.8	668.0	659.4	667.9
	2264.8	626.0	0.7793	0.1390	672.7	672.3	670.8	671.8
	2265.2	625.9	0.7800	0.1766	676.7	676.3	680.7	675.9
	2264.6	623.6	0.7832	0.2265	681.7	681.3	694.6	681.0
	2264.3	626.6	0.7775	0.2487	683.9	683.6	704.7	683.3
	2263.8	626.9	0.7756	0.2792	686.9	686.6	755.8	686.4
	2261.9	625.6	0.7763	0.3196	690.7	690.4	780.2	690.2
	2261.8	625.8	0.7773	0.3626	694.7	694.5	808.3	694.4
	2262.1	620.9	0.7890	0.3852	697.1	696.8	826.6	696.7
	2261.5	628.9	0.7704	0.4087	699.3	699.1	837.7	699.0
	2261.1	624.2	0.7815	0.4269	701.0	700.8	845.8	700.8
	2261.7	625.4	0.7766	0.4503	703.2	703.0	857.7	702.9
	2261.9	626.1	0.7744	0.4894	706.8	706.4	876.0	706.4
	2261.8	625.8	0.7748	0.5090	709.1	708.7	784.6	708.9
	2260.8	626.4	0.7725	0.5281	711.1	710.6	764.8	710.8
110a	2265.0	515.1	1.4317	0.0988	547.2	507.6	545.2	545.2
	2260.9	552.0	1.3671	0.1017	584.5	583.9	584.5	584.6
	2265.4	552.2	1.3668	0.1344	596.0	595.3	595.9	596.4
	2264.9	553.7	1.3641	0.1717	611.1	609.8	610.6	611.2
	2264.4	553.2	1.3649	0.2219	627.9	626.7	628.2	629.0
	2259.0	550.0	1.3709	0.2438	633.3	631.7	632.9	633.6
	2265.2	550.5	1.3701	0.2725	644.2	642.0	643.3	644.0
	2259.4	553.0	1.3652	0.3128	660.2	658.3	660.3	661.1
	2263.6	553.6	1.3642	0.3559	676.5	673.5	675.0	676.2
	2264.4	551.6	1.3680	0.3785	680.6	679.6	682.8	684.1
	2264.6	550.9	1.3693	0.4024	689.3	685.8	687.8	688.6
	2263.0	550.7	1.3696	0.4200	693.6	691.7	693.7	694.4
	2258.3	552.2	1.3668	0.4441	699.4	698.1	699.3	699.5
	2262.2	551.6	1.3679	0.4618	702.6	701.7	702.2	702.3
	2262.2	550.2	1.3705	0.4809	705.0	704.3	704.5	704.6
110b	2257.9	617.8	1.2231	0.1048	653.6	653.2	653.8	654.5
	2262.8	619.0	1.2198	0.1383	666.2	666.0	666.9	667.9
	2263.7	620.3	1.2158	0.1761	675.2	674.9	674.5	674.4
	2258.1	623.4	1.2062	0.2265	680.1	679.9	679.5	679.5
	2260.5	624.8	1.2020	0.2485	682.6	682.3	681.9	681.8
	2264.6	623.1	1.2074	0.2766	685.4	685.2	684.9	684.8
	2264.1	622.0	1.2107	0.3162	689.6	689.3	688.9	688.8
	2258.8	621.1	1.2132	0.3807	696.1	695.7	695.4	695.3
	2261.6	623.2	1.2071	0.4035	698.3	697.9	697.5	697.5
	2261.8	621.1	1.2134	0.4211	699.9	699.6	699.3	699.3
	2255.0	621.3	1.2124	0.4436	702.2	701.9	701.5	701.4
	2259.0	621.7	1.2114	0.4624	704.0	703.7	703.3	703.2
	2257.2	621.8	1.2111	0.4819	705.7	705.5	705.1	705.0
	2259.1	628.4	1.1901	0.5245	710.0	709.7	709.2	709.2
111a	2264.3	548.1	1.3802	0.1011	579.5	581.6	580.2	582.3
	2265.6	547.6	1.3811	0.1343	590.6	592.7	591.1	593.4
	2265.7	549.7	1.3772	0.1719	605.2	608.7	606.5	609.8

Table B.2 continued

Experiment	P psi	T_{in} °F	G Mlbm/hr/ft^2	q'' Mbtu/hr/ft^2	T_1 °F	T_2 °F	T_3 °F	T_4 °F
	2269.9	554.1	1.3690	0.2216	629.2	633.9	631.0	634.9
	2261.2	550.8	1.3751	0.2435	633.8	637.3	634.7	639.6
	2263.7	547.9	1.3805	0.2721	641.7	647.6	643.3	649.0
	2264.7	547.2	1.3820	0.3129	654.9	661.3	657.1	664.2
	2265.4	549.1	1.3784	0.3553	671.3	675.6	673.0	677.7
	2264.8	550.3	1.3761	0.3788	680.0	685.1	681.9	687.6
	2265.9	552.0	1.3728	0.4016	688.7	691.8	689.2	693.9
	2265.6	551.6	1.3737	0.4194	693.7	696.2	694.5	697.6
	2264.3	550.4	1.3758	0.4439	699.4	699.5	698.2	700.6
	2265.9	550.4	1.3758	0.4627	702.3	701.5	700.6	702.5
	2264.0	552.0	1.3729	0.4812	704.7	703.6	702.8	704.5
	2263.5	552.3	1.3722	0.5251	709.1	707.8	707.0	708.9
111b	2263.7	625.5	1.2071	0.1048	665.7	666.1	665.6	666.6
	2256.9	626.0	1.2053	0.1756	674.8	674.0	673.8	674.6
	2258.7	621.1	1.2209	0.3165	690.0	689.0	688.5	690.4
	2266.4	618.5	1.2291	0.3589	693.8	692.9	692.1	694.0
	2228.1	620.1	1.2226	0.3798	694.3	693.2	692.5	694.9
	2228.7	621.3	1.2187	0.4032	696.2	695.2	694.5	696.8
	2264.5	617.1	1.2329	0.4209	700.1	699.1	698.2	700.7
	2262.7	620.6	1.2224	0.4446	702.6	701.5	700.6	703.2
	2224.0	622.1	1.2162	0.4623	702.6	701.5	700.5	703.5
	2260.5	619.7	1.2250	0.4804	704.6	703.4	702.4	704.7
	2260.1	623.7	1.2129	0.5250	710.3	709.3	708.1	711.5

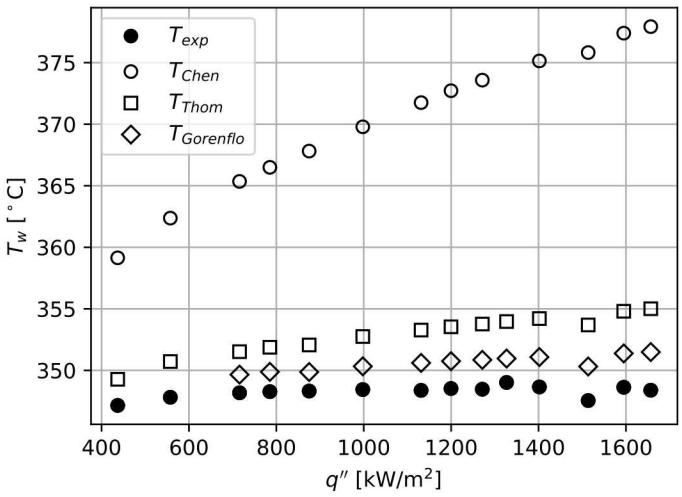

q'' kW/m^2	$T_{w,exp}$ °C	$T_{w,chen}$ °C	$T_{w,thom}$ °C	$T_{w,gor}$ °C
437	347.2	359.1	349.3	–
557	347.8	362.4	350.7	–
716	348.2	365.4	351.5	349.7
785	348.3	366.5	351.9	349.9
875	348.3	367.8	352.1	349.9
998	348.4	369.8	352.8	350.3
1131	348.4	371.8	353.3	350.6
1200	348.5	372.7	353.5	350.8
1271	348.5	373.6	353.8	350.9
1327	349.0	–	354.0	351.0
1402	348.7	375.1	354.2	351.1
1514	347.5	375.8	353.7	350.3
1595	348.6	377.4	354.8	351.4
1657	348.4	377.9	355.0	351.5

Figure B.1: CTF and experimental results for WALT rod 80

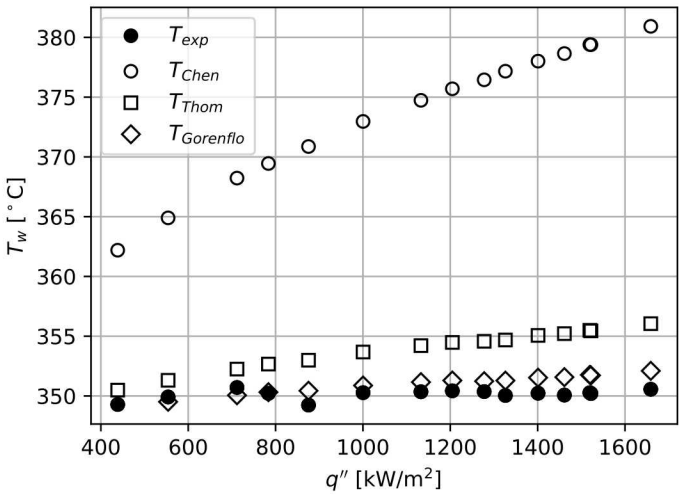

q'' kW/m^2	$T_{w,exp}$ °C	$T_{w,chen}$ °C	$T_{w,thom}$ °C	$T_{w,gor}$ °C
438	349.3	362.2	350.5	–
554	349.9	364.9	351.3	349.5
712	350.7	368.2	352.2	350.1
784	350.2	369.4	352.7	350.3
875	349.2	370.9	353.0	350.4
1000	350.3	373.0	353.7	350.9
1133	350.4	374.7	354.2	351.2
1205	350.4	375.7	354.5	351.3
1278	350.4	376.4	354.6	351.2
1326	350.0	377.2	354.7	351.3
1401	350.2	378.0	355.1	351.5
1461	350.1	378.6	355.2	351.6
1520	350.3	379.4	355.5	351.8
1522	350.2	379.4	355.4	351.7
1659	350.6	380.9	356.0	352.1

Figure B.2: CTF and experimental results for WALT rod 86

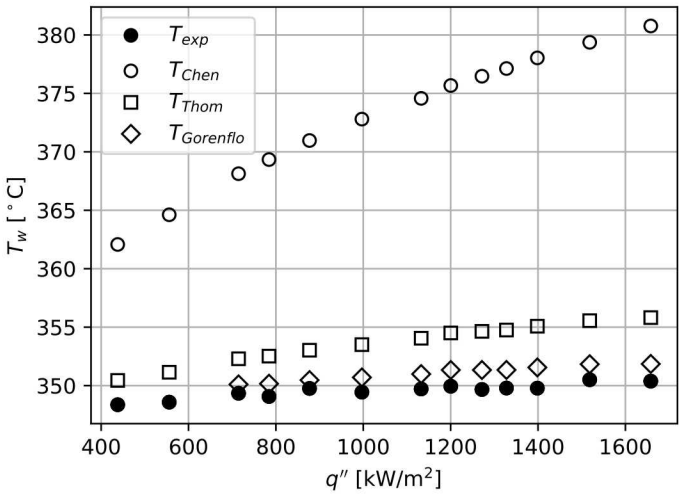

q'' kW/m^2	$T_{w,exp}$ °C	$T_{w,chen}$ °C	$T_{w,thom}$ °C	$T_{w,gor}$ °C
438	348.4	362.1	350.4	–
556	348.6	364.6	351.1	–
715	349.3	368.1	352.3	350.1
784	349.1	369.3	352.5	350.2
877	349.8	371.0	353.0	350.5
997	349.4	372.8	353.5	350.7
1132	349.7	374.6	354.1	351.0
1200	349.9	375.7	354.5	351.3
1272	349.7	376.5	354.6	351.3
1328	349.8	377.1	354.8	351.3
1398	349.8	378.0	355.1	351.6
1518	350.5	379.4	355.6	351.8
1658	350.4	380.8	355.8	351.9

Figure B.3: CTF and experimental results for WALT rod 87

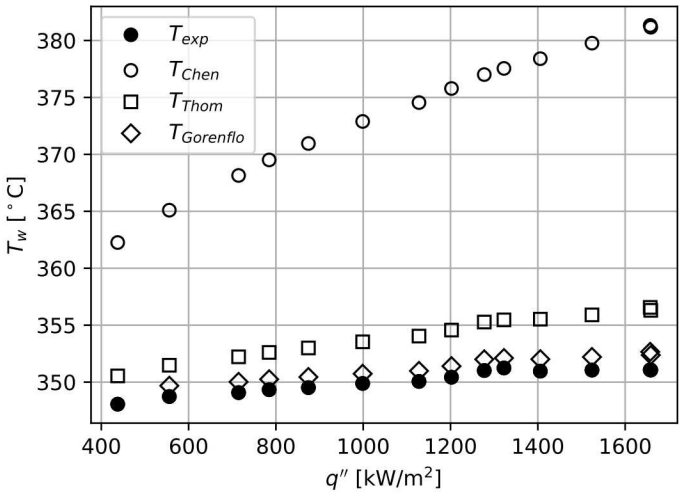

q'' kW/m^2	$T_{w,exp}$ °C	$T_{w,chen}$ °C	$T_{w,thom}$ °C	$T_{w,gor}$ °C
438	348.1	362.3	350.5	–
556	348.7	365.1	351.5	349.7
715	349.1	368.1	352.2	350.0
785	349.3	369.5	352.6	350.3
874	349.5	371.0	353.0	350.4
999	349.9	372.9	353.5	350.7
1128	350.1	374.5	354.0	351.0
1202	350.4	375.8	354.6	351.4
1277	351.0	377.0	355.3	352.0
1322	351.2	377.5	355.5	352.1
1406	351.0	378.4	355.5	352.0
1524	351.1	379.8	355.9	352.2
1657	351.1	381.3	356.6	352.7
1659	351.1	381.2	356.3	352.4

Figure B.4: CTF and experimental results for WALT rod 88

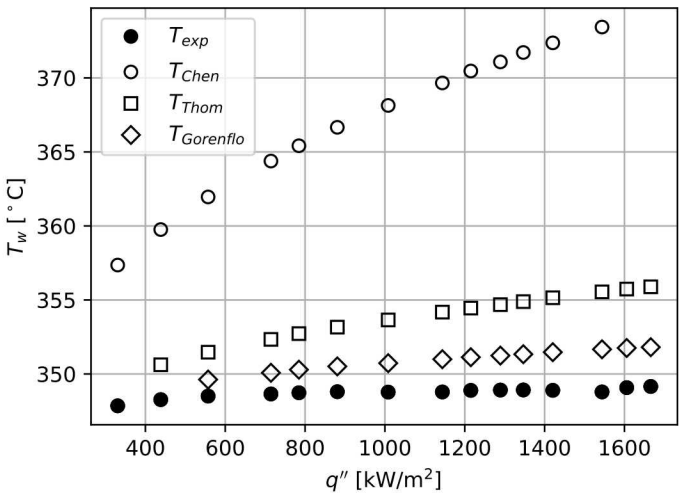

q'' kW/m^2	$T_{w,exp}$ °C	$T_{w,chen}$ °C	$T_{w,thom}$ °C	$T_{w,gor}$ °C
331	347.8	357.4	–	–
438	348.3	359.8	350.6	–
557	348.5	362.0	351.5	349.6
715	348.6	364.4	352.3	350.1
785	348.7	365.4	352.7	350.3
881	348.8	366.7	353.2	350.5
1008	348.8	368.1	353.6	350.7
1144	348.8	369.7	354.2	351.0
1215	348.9	370.5	354.5	351.1
1289	348.9	371.1	354.7	351.2
1347	348.9	371.7	354.9	351.3
1421	348.9	372.4	355.1	351.5
1544	348.8	373.4	355.5	351.7
1606	349.1	–	355.7	351.8
1666	349.2	–	355.9	351.8

Figure B.5: CTF and experimental results for WALT rod 94

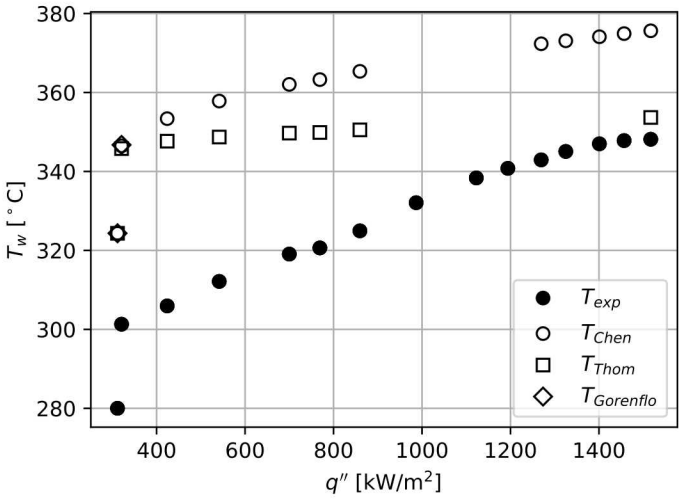

q'' kW/m^2	$T_{w,exp}$ °C	$T_{w,chen}$ °C	$T_{w,thom}$ °C	$T_{w,gor}$ °C
312	280.0	324.3	324.3	324.3
321	301.3	346.5	345.8	346.7
424	305.9	353.4	347.7	–
542	312.1	357.8	348.7	–
700	319.1	362.0	349.7	–
769	320.6	363.3	349.9	–
860	325.0	365.4	350.5	–
987	332.1	–	–	–
1123	338.4	–	–	–
1194	340.8	–	–	–
1269	342.9	372.3	–	–
1325	345.1	373.1	–	–
1401	347.0	374.1	–	–
1457	347.8	374.9	–	–
1517	348.2	375.6	353.7	–

Figure B.6: CTF and experimental results for WALT rod 110a

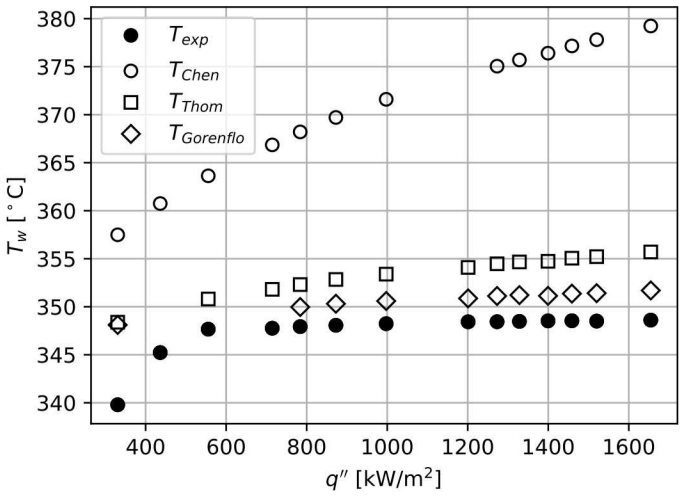

q'' kW/m^2	$T_{w,exp}$ °C	$T_{w,chen}$ °C	$T_{w,thom}$ °C	$T_{w,gor}$ °C
331	339.8	357.5	348.4	348.1
436	345.2	360.7	–	–
556	347.7	363.6	350.8	–
715	347.8	366.9	351.8	–
784	347.9	368.2	352.3	350.0
873	348.1	369.7	352.8	350.3
997	348.2	371.6	353.4	350.6
1201	348.4	–	354.1	350.9
1273	348.4	375.1	354.5	351.1
1328	348.5	375.7	354.7	351.2
1399	348.5	376.4	354.7	351.1
1459	348.5	377.2	355.1	351.4
1520	348.5	377.8	355.2	351.4
1655	348.6	379.2	355.7	351.7

Figure B.7: CTF and experimental results for WALT rod 110b

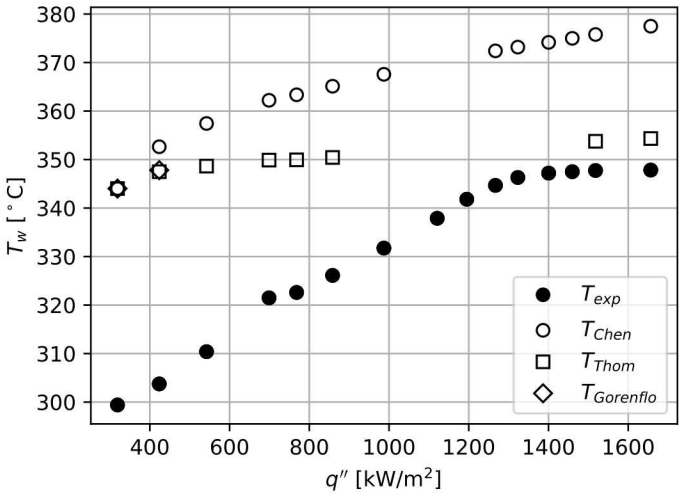

q'' kW/m^2	$T_{w,exp}$ °C	$T_{w,chen}$ °C	$T_{w,thom}$ °C	$T_{w,gor}$ °C
319	299.4	344.0	344.0	344.0
424	303.7	352.6	347.5	347.8
542	310.4	357.4	348.6	–
699	321.5	362.2	349.9	–
768	322.6	363.4	349.9	–
858	326.1	365.1	350.4	–
987	331.7	367.6	–	–
1121	337.9	–	–	–
1195	341.8	–	–	–
1267	344.7	372.4	–	–
1323	346.3	373.2	–	–
1400	347.2	374.2	–	–
1460	347.5	375.0	–	–
1518	347.7	375.8	353.8	–
1656	347.8	377.5	354.3	–

Figure B.8: CTF and experimental results for WALT rod 111a

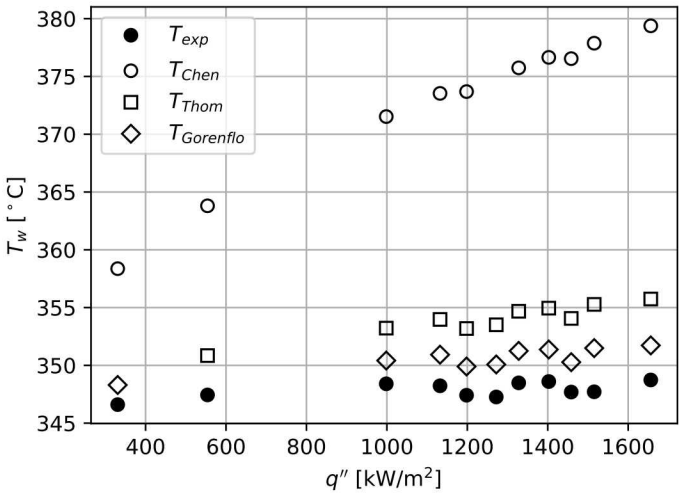

q'' kW/m^2	$T_{w,exp}$ °C	$T_{w,chen}$ °C	$T_{w,thom}$ °C	$T_{w,gor}$ °C
331	346.6	358.4	–	348.3
554	347.4	363.8	350.8	–
998	348.4	371.5	353.2	350.4
1132	348.2	373.5	354.0	350.9
1198	347.4	373.7	353.2	349.9
1272	347.3	–	353.5	350.1
1328	348.5	375.7	354.7	351.3
1403	348.6	376.7	355.0	351.4
1458	347.7	376.5	354.1	350.3
1515	347.7	377.9	355.3	351.5
1656	348.7	379.4	355.7	351.7

Figure B.9: CTF and experimental results for WALT rod 111b